IDENTIFICATION OF SAND DUNES IN THE EARLY JURASSIC AGED NUGGET SANDSTONE FORMATION IN THE MOXA ARCH OF WYOMING USING SEISMIC ATTRIBUTES, PETROPHYSICAL MODELING, AND SEISMIC DATA CONDITIONING

APPROVED BY SUPERVISORY COMMITTEE:

_____

Dr. Sumit Verma, Ph.D.
Chair

_____

Dr. Mohamed Zobaa, Ph.D.

_____

Dr. Miles A. Henderson, Ph.D.

_____

Dr. Kurt J. Marfurt, Ph.D.

_____

Dr. Shawn Watson, Ph.D.
Graduate Faculty Representative

IDENTIFICATION OF SAND DUNES IN THE EARLY JURASSIC AGED NUGGET SANDSTONE FORMATION IN THE MOXA ARCH OF WYOMING USING SEISMIC ATTRIBUTES, PETROPHYSICAL MODELING, AND SEISMIC DATA CONDITIONING

By

DHRUV AGRAWAL, M.S.

THESIS

Presented to the Graduate Faculty of Geology of

The University of Texas Permian Basin

In Partial Fulfillment

Of Requirements

For the Degree of

MASTER OF SCIENCE

THE UNIVERSITY OF TEXAS PERMIAN BASIN

May 2019

ACKNOWLEDGMENTS

I would like to thank my mentor and thesis advisor, Dr. Sumit Verma, for his guidance and support during my two years here and giving me the opportunity to do this wonderful project. I would like to express my gratitude to my other committee members, Dr. Mohamed Zobaa, Dr. Miles A. Henderson, Dr. Kurt J. Marfurt, and Dr. Shawn Watson for their continuous support and constructive feedback to finish this research.

I am truly grateful to the United States Department of Energy (Contract No: DE-FE0023328) which provided the research grant to acquire the seismic data and Dr. Mallick (University of Wyoming) who shared the dataset with UT Permian Basin. This research would not have been possible without the dataset which formed the basis of this project.

I would also like to acknowledge my friends and colleagues Brady Lujan, Matthew Scipione, Fatimah Adelekan, Joanna Walker and Yvonne Iwo-Brown who helped me out in completing this research at various stages of the project.

Seismic attributes were computed using AASPI consortium software. Seismic inversion was performed on HampsonRussell of CGG GeoSoftware. 3D seismic interpretation was completed using Petrel software of Schlumberger. Well to seismic tie was performed on RokDoc from Ikon Science.

Lastly, I would like to express my most sincere gratitude to my family and friends for their constant support in all these years. They made my time memorable here and kept me going. This accomplishment would not have been possible without them.

ABSTRACT

The Green River Basin in the SW Wyoming is responsible for all the hydrocarbon production within Lincoln, Sublette, Sweetwater, and Uinta Counties in Wyoming. NW-SE lineations with peculiar shapes, referred as funny looking things (FLTs), exist in the seismic data from Lincoln County, associated with the Triassic/Jurassic deposition in the Moxa Arc. The Moxa Arch has been an important geologic structure for hydrocarbon exploration since the mid-1940s. It is also said to be one of the two carbon sequestration sites present in Wyoming. The Nugget Sandstone formation, wherein these FLTs lie, is an eolian sandstone that was deposited as part of the Early Jurassic sand sea that covered Arizona, Utah, and southwestern Wyoming.

Seismic attributes are used to enhance subtle features, aid in explanation of the depositional environment, and to delineate minor faults, folds, structural or stratigraphic traps and discontinuities. The peculiar features seen in the seismic data cannot be explained by acquisition and processing errors which led to finding a geologic explanation. Well to seismic ties on three wells surrounding the seismic survey indicated that the observed FLTs on seismic correspond to the Early Jurassic aged Nugget Sandstone. In the Early Jurassic time period, Wyoming was situated around 25^{o} latitude, at a subtropical dessert forming location. The Nugget Sandstone is predominantly eolian sandstone. The structural curvature attribute illuminated the presence of northwest-southeast trending linear geologic features related to the sand dunes in the Nugget Sandstone formation. Coherence anomalies demarcated the boundaries of the dune sandstones and interdune deposits.

Seismic inversion and the petrophysical models determined that the dune deposits are low impedance high porosity sands whereas the inter-dune deposits consist of high impedance impermeable evaporites like anhydrite and halite. Co-rendering the seismic attributes and inversion results displayed the extent and nature of the eolian dunes within the 3D seismic volume. Seismic data conditioning improved the signal to noise ratio and the discontinuities are sharper after applying a structural-oriented filter. A paleo-wind direction of approximately N 225˚ was calculated based on the average direction of these lineaments.

TABLE OF CONTENTS

LIST OF FIGURES

is more representative of a sand dunal environment, whereas the well A suggests more of an interdunal environment (Verma et al., 2018).

Figure 14: Stratal slices of the coherence attribute, 1 represents maximum similarity and 0 represents maximum dissimilarity. The eolian dune lineaments begin to appear 24 ms below Nugget (c), become prominent around 44 ms (b), and then start disappearing about 64 ms below Nugget (a). Note the blue arrow indicates the inter-dunal whereas the yellow arrow indicates the well-developed sand dunes.

Figure 15: Stratal slices of most positive curvature (k_1), co-rendered with most negative curvature (k_2) and coherence. All slices are taken with respect to the Nugget Sandstone reflector. The eolian dune lineaments begin to appear 24 ms below Nugget (c), become prominent around 44 ms (b), and then start disappearing about 64 ms below Nugget (a).

Figure 16: GLCM Homogeneity applied with a bump map (the red arrows illuminate the stoss side of the dunes with gradual dip)

Figure 17: Left – sphere without bump mapping, Middle - bump map to be applied to the sphere, Right – sphere with bump mapping. Notice how the big black dot appears as the big bump on the right while other smaller dots generate smaller bumps. This is achieved by changing how an illuminated surface reacts to light, without modifying the size or shape of the surface.

Figure 18: Stratal slices of P-Impedance (Z_p) co-rendered with coherence attribute. All slices are taken with respect to the Nugget Sandstone reflector. The eolian dune lineaments begin to appear 24 ms below Nugget (c), become prominent around 44 ms (b), and then

start disappearing about 64 ms below Nugget (a). Note the blue arrow indicates the inter-dunal whereas the yellow arrow indicates the well-developed sand dunes. The co-rendered figure of curvature and coherence implies that the distinct features seen in coherence slices are surrounded by antiforms and synforms.

Figure 19: Stratal slices of the seismic facies, generated with self-organizing map algorithm (SOMs). All slices are with respect to the Nugget Sandstone top, the eolian dunes lineaments start appearing 66 ms below Nugget (a), become prominent (b) and then start disappearing around 26 ms below Nugget (c). Based on the correlation of P-impedance with seismic facies, blue colored facies represent interdunal deposits (evaporites) while yellow colored facies represent dunal deposits (sands).

Figure 20: (Top) The discontinuity surfaces obtained by applying Ant Track workflow (Silva et al., 2005) on curvature k_1 volume (Figure). Note that all the small north to east striking lineaments were filtered out (Verma et al., 2018).

Figure 21: (Bottom) The rose diagram, showing the derived direction; which is simply the strike direction of the lineaments (Verma et al., 2018).

Figure 22: Seismic acquisition with 6 folds, S stands for source and R for receiver

Figure 23: Pre-stack data before (red) and after (green) NMO correction (course slides)

Figure 24: All traces of a single common midpoint stacked together to a single trace with reduced incoherent noise and improved signal to noise (S/N) ratio (UTPB course slides)

Figure 31: Stratal slices of the Coherence attribute before and after the seismic data conditioning (both are 24 ms below Nugget). The green arrows indicate the features which look sharper and more resolved after applying structure-oriented filter (SOF).

Figure 32: Satellite image of Rub' al Khali, Arabia – one of the largest desert in the world. The white arrow shows wind direction, brown color shows dunes and blue/white color shows interdunes (modified after ASTER, 2005). The stars represent the approximate analogical relative location of wells A and C in a dunal/interdunal deposit area.

CHAPTER 1

INTRODUCTION

Different seismic attributes can concentrate and better interpret distinct geological and stratigraphic features in the geology of an area. For example, amplitude and frequency attributes can show stratigraphic changes. Geometric attributes such as dip, curvature, and convergence are better for finding out reflector morphology. Some seismic attributes are better indicators of edges of seismic facies and others are the optimum choices for measuring the facies themselves (Chopra and Marfurt, 2007).

While looking at different seismic attributes used to be sufficient in earlier days, recent developments in computational geophysics allow multiple attributes to be layered or co-rendered over each other enabling visualization or identification of seismic facies that would have otherwise been overlooked by even the best of geophysicists (Roy et al., 2013; Zhang et al., 2015; Zhao et al., 2016).

This thesis describes the peculiar seismic features identified in the Early Jurassic Nugget Sandstone formation in the Moxa Arch located in southwestern Wyoming, west of Green River Basin. They are broken reflectors unlike anything else seen in the seismic survey and there are no faults above or below these features which could explain their geology or the formation. At the beginning of the study, they were referred to as “funny looking things” (FLTs).

After going through the calculation of seismic attributes and petrophysical analysis, the formation was identified as Nugget Sandstone. The past studies (Parrish and Peterson, 1988; Chan and Archer, 2000; Loope and Rowe, 2003) have mentioned the sand dunes in Navajo Sandstone, which is the equivalent of Nugget in Utah and Arizona. The wind direction was found out by looking at the outcrops in these areas, measuring strikes and dips, and drawing dipoles indicating corresponding wind direction on each of these outcrops. After calculating the average direction of these dipoles, the general wind direction was identified as represented by blue arrows in Figure 1. This study arrives at the same result with seismic data and well logs which has been done rarely in the past.

Chapter 2 discusses the geology of the Moxa Arch in Wyoming. It explains the thickness and geologic setting of Nugget Sandstone and Moxa Arch in general with respect to other formations in the region in brief detail.

Chapter 3 follows with the description of the available data which was shared with me by University of Wyoming for the collaboration of research projects with UT Permian Basin. Chapter 4 details the formation, geomorphic characteristics and the various types of sand dunes. It discusses the primary factors involved in dune formation. Chapter 4 also shows an example of how sand dunes look like in outcrops as I visited Arches National Park to get a deeper understanding of them.

Chapter 5 explains the importance and application of seismic attributes in the modern geophysics as well as in this study. It details the well to seismic tie along with

seismic inversion. This chapter also explains the attributes in a comprehensive manner, while also showing results of the same on this dataset.

Chapter 6 explains the basic difference between seismic processing and seismic conditioning. It explains a few conditioning as well as processing steps, which were executed after receiving the pre-stack data. The data after the conditioning looks much sharper and better than before.

Chapter 7 presents the final results and discussions of this study. It also discusses in minor detail the modern-day analog that was very helpful in visualizing the dataset as well as future work that can and should be done on this dataset.

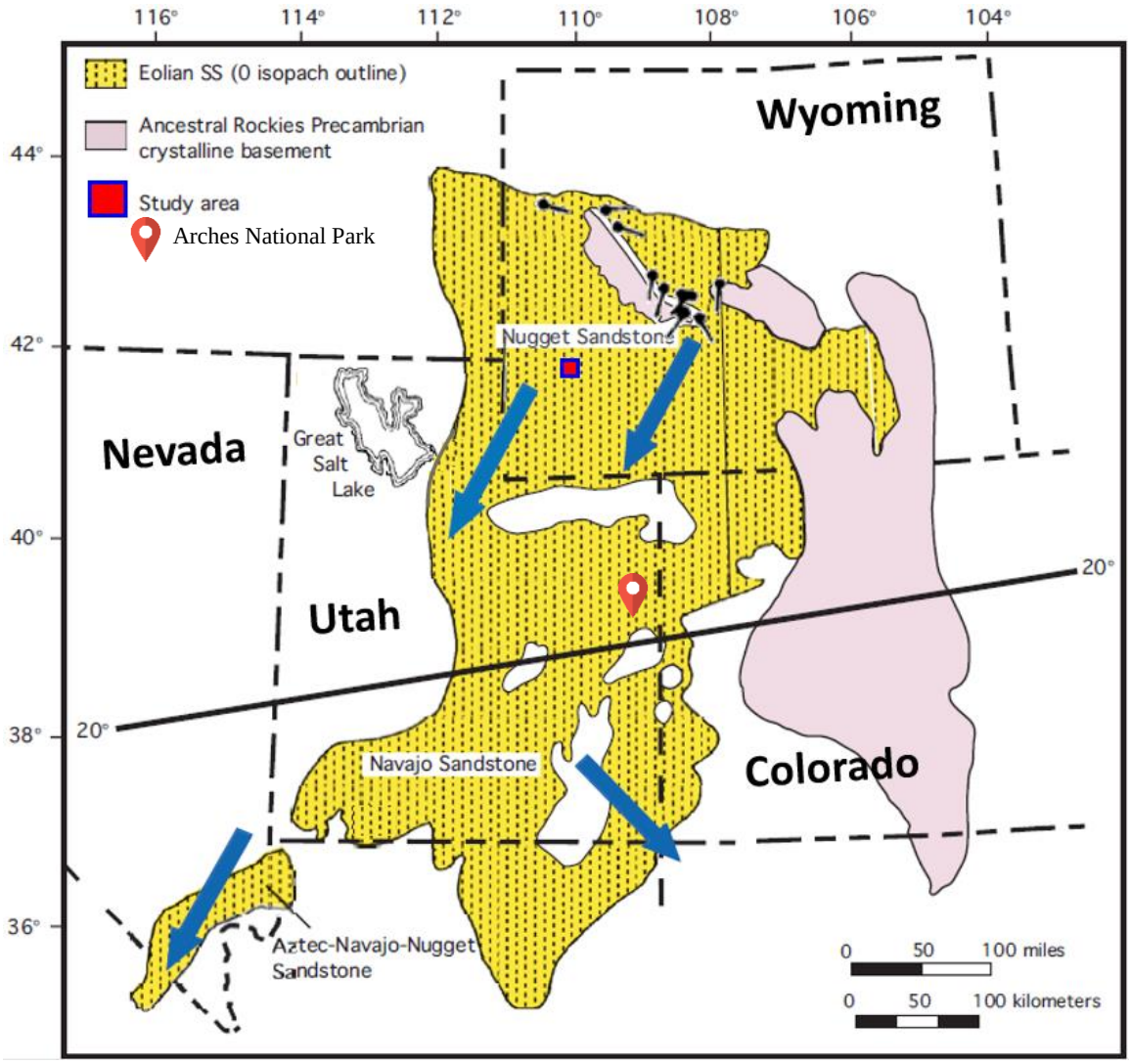

Figure 1: Paleo wind direction of Nugget and Navajo Sandstone. Note the black dipoles in Wyoming state close to Precambrian uplift showing the outcrop locations of Nugget Sandstone where the wind direction measurement was taken (after Parrish and Peterson, 1988; Chan and Archer, 2000). The blue arrows show the general wind direction. Please refer to Figure 9 for the significance of the Arches National Park here.

CHAPTER 2

GEOLOGY OF THE STUDY AREA

The Moxa Arch, located west of Green River Basin and Rock Springs Uplift, is a doubly plunging anticline formed during early stage of the Laramide orogeny. The Moxa Arch dips gently (~5˚) and extends from beneath the Uinta Mountains at the Utah/Wyoming border, north to the town of La Barge, Wyoming, where it turns northwest and plunges beneath the western Wyoming fold-and-thrust belt. The Wyoming thrust belt, developed during Laramide orogeny, has a well-documented structural history that indicates uplift along a basement-involved thrust fault beginning in the Late Cretaceous and continuing through the Early Eocene (Campbell-Stone et al. 2011, Verma et al., 2016). The Moxa Arch has been the target of extensive hydrocarbon exploration since the 1960s because of its size and structural closure with major gas and oil reservoirs being discovered all along the arch (Lindquist, 1983).

In this study, the focus is on the structures of the Moxa Arch based on seismic attributes and seismic inversion. One of such formations that harbors the seismic structures in question is the Nugget Sandstone that shows minimal faulting in the formation, a regional unconformity at its top and base and is of Lower Jurassic age (Picard, 1997). The Nugget Sandstone is about 500 ft thick and its top dips from about 12,500 ft in the North to about 13,500 ft in the South of our dataset.

Moxa Arch contains approximately 22,000 ft (6.7 km) of sedimentary strata deposited on Precambrian basement (Verma et al., 2018). The Mississippian Madison

Limestone and Jurassic Nugget Sandstone are potential reservoir formations for CO_2 sequestration (Grana et al., 2017; Mallick and Adhikari, 2015; Surdam, 2013). In the study area, the Nugget Sandstone lies around 12,500 ft (3.8 km) below the surface, and the Madison Limestone around 16,500 ft (5 km) below the surface.

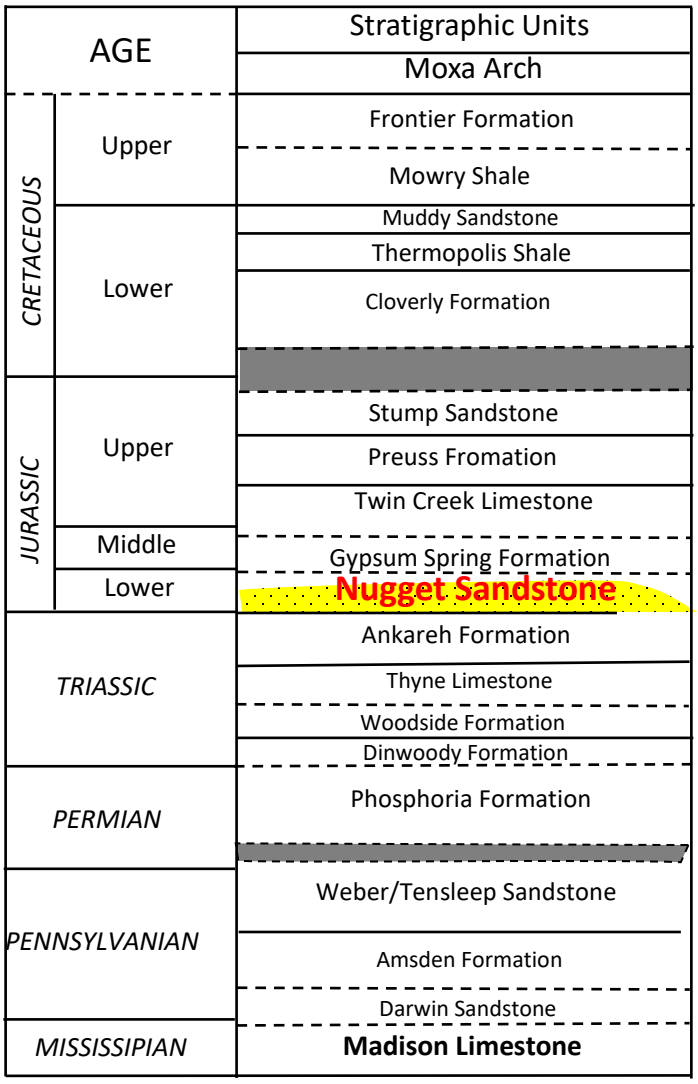

Figure 2: Generalized stratigraphy of the Moxa Arch (modified after Thyne et al., 2010)

CHAPTER 3

METHODS

The 3D seismic dataset from Moxa Arch was acquired with the research grant provided by the United States Department of Energy along with three wells Keller 1-12, AGI 3-14 and AGI 2-18. The seismic survey area is surrounded by the Wyoming-Idaho-Utah Thrust Belt in the west, the La Barge Platform in the north and the Green River Basin in the east. Figure 3 shows the relative position of the seismic survey and the three wells that were used for this research. The area of the survey is about 36 square miles and was acquired in 1999 with a dynamic source and 5 second record length with a maximum offset range of 14,500 ft.

The interesting features are present below 2200 milliseconds (ms) two-way time in the seismic data and extend to about 2300 ms. A horizon was picked along the top surface or boundary of the features (Figure 4). The vertical thickness of the features remain almost same everywhere in the seismic data; however, the features are not at the same depth everywhere. The top of the features dip down from 2200 ms to around 2350 ms going from the North end to the South end of the survey.

Seismic attributes were calculated to understand the extent and nature of the peculiar features. The main attributes focused on in the beginning were coherence (sobel filter) and curvature. Coherence is an edge detection attribute commonly used now in image-processing software programs and demarcates the discontinuities present on a surface. Curvature is a geometric attribute which shows the rate of change of dip of a

surface and hence is used to notice the synforms and antiforms on a surface while also showing how steep the dip angles are. For the purpose of this study, Keller 1-12 is referred to as well A, AGI 3-14 as well B and AGI 2-18 as well C.

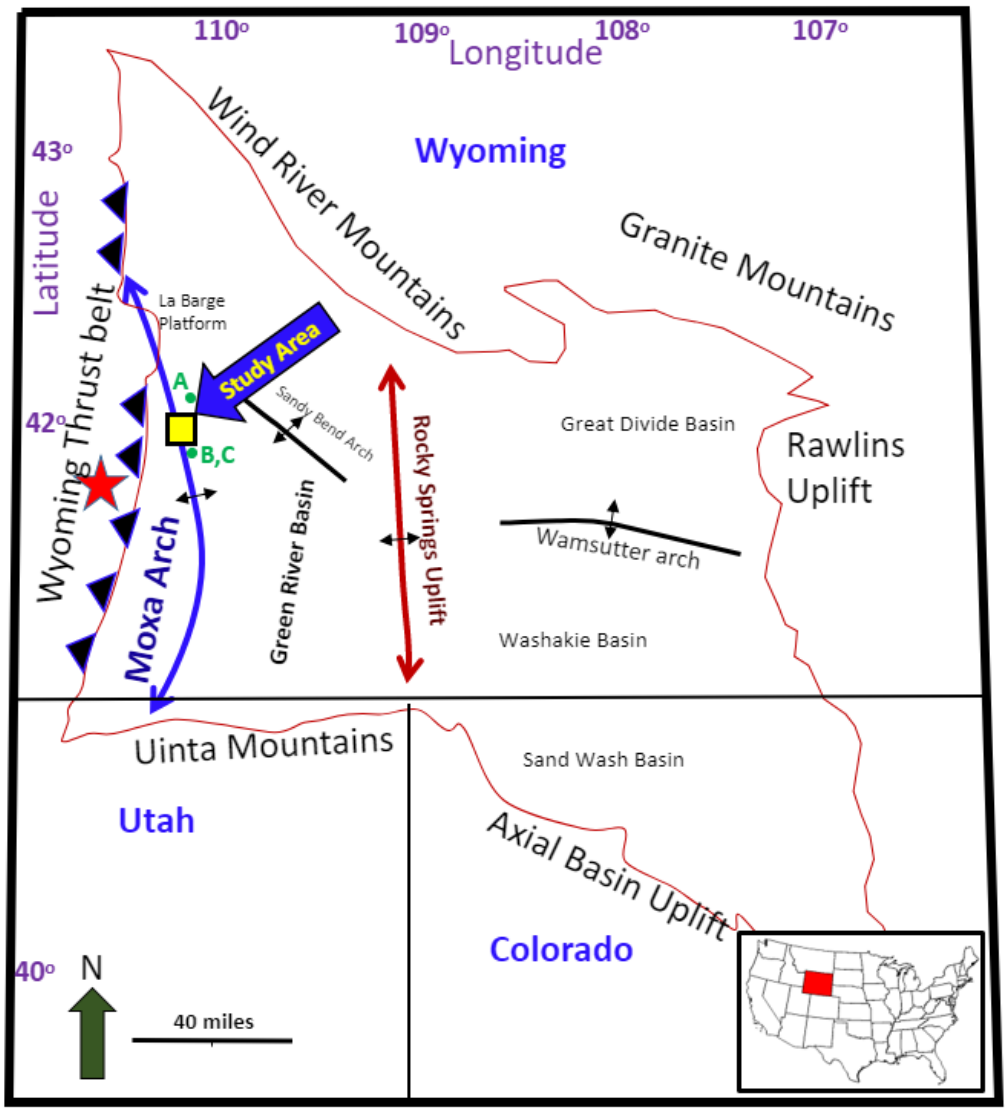

Figure 3: Location map of the Moxa Arch and Rock Springs Uplift in SW Wyoming (modified after Verma et al., 2016). A, B and C are the wells used for the study. Red star indicates the Naughton Power Plant.

In a seismic study, structural features are evident in the normal section but to look at the stratigraphic features, the seismic data is flattened on the horizon of the formation top. Flattening the seismic volume negates the effect of the regional dip which gets added to the stratigraphic dip and gives an illusion of increased dips everywhere in the section. So, after the volume was flattened along the horizon of interest (the one that was picked earlier), the attributes were studied. By looking at the stratal time slices, the features appeared like sand dunes with interdune areas between them.

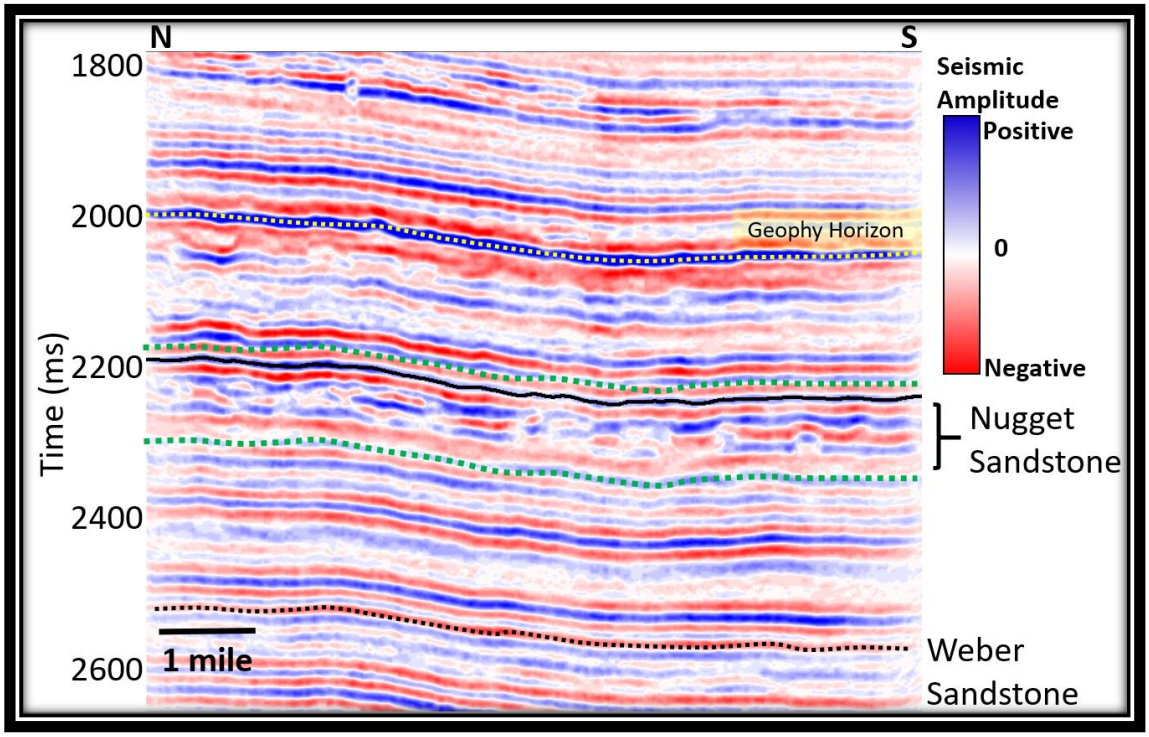

Figure 4: Seismic amplitude vertical (north-south) section. The Nugget formation is approximately 75 ms thick. The geophysical horizon on top is a very distinct seismic reflector below the Mowry Formation (Verma et al., 2018).

To confirm the nature of the features, the formation type and mineral composition was required. So, well to seismic tie was performed on all 3 wells. The well to seismic tie correlation was about 54% for well B, about 57% for well C and the highest correlation of about 62% for well A which is pretty significant. The formation was confirmed to be Nugget Sandstone which is an Early Jurassic formation and is famously known by Navajo Sandstone in other areas. Figure 5 shows the Early Jurassic paleo-geographic map with the relative position of the seismic survey. The survey area appears to be surrounded by huge sand bodies during that age which bolsters the primary lithologic interpretation of the formation to be sandstone.

The petrophysical analysis of the wells with conventional logs – gamma ray, bulk density and neutron density exhibit the mineral composition of the formation. To delve deeper into the types of sand dunes, seismic inversion was performed to get the P-impedance and GLCM homogeneity was used with bump map and self-organizing maps to delineate the seismic facies in the zone of interest.

The Ant Track workflow was applied on the curvature k_1 volume to get more information about the wind current involved in the formation of the sand dunes. The rose diagram (Figure 21) was calculated to show the exact wind direction by adding up the perpendicular directions to the strikes of the lineaments seen in the Ant Track workflow (Verma et al., 2018).

After the pre-stack seismic data was received, seismic conditioning was performed on it including few processing steps like NMO correction, stacking and structure-oriented

filter. The newly conditioned data looks much sharper than before and can be used for future work.

Figure 5: North American continent during Early Jurassic (after National Park Services, 2018)

CHAPTER 4

FORMATION OF SAND DUNES, GEOMORPHIC CHARACTERISTICS AND TYPES

Sand dune can be defined as any accumulation of sand (Augustyn et al., 2017) grains shaped into a mound or ridge by the wind (Augustyn et al., 2019) under the influence of gravity (Faller et al., 2019). Whenever a fluid moves over an unconsolidated sediment, loose sand is windblown, and dunes are formed. This can happen in deserts, beaches or even some eroded and abandoned farm fields in semiarid regions. There can also be subaqueous dunes on the beds of rivers and tidal estuaries, or sand waves on the continental shelves beneath shallow seas. There are instances from Mars (Malin et al., 2019) that show dunes widely distributed in both craters and in a sand sea surrounding the north polar ice cap (Breed et al., 2019).

True dunes are different from the ones associated with vegetation. The former cover more extensive areas. If a sand dune has low relief and gently undulating surfaces, then it is called sand sheet. Sand dunes are generally formed in the condition of very low rainfall. Often, sand dunes are also associated with high bioturbation which increases the porosity of the sands too (Loope and Rowe, 2003). A deep understanding of sand dunes requires a basic knowledge of their sands, the winds, and the interactions of these main elements.

Sands

Dunes are mostly formed of sand sized particles. The clay (Augustyn, et al., 2019) particles are too tight and, if picked up by wind, are lifted high into the air unless they are aggregated into sand sized particles in which case they can be formed into dunes. Silt particles are too light and get blown away faster than sand. On the contrary, particles bigger than sand like pebbles only form into dune-like features and have to be carried by very strong and persistent winds. Even bigger rocks like boulders can only be moved by wind on slippery surfaces like ice or wet saline mud and never form into dunes (Breed et al., 2019).

Generally, the grain diameters of the sands in the dunes is between 0.02 and 0.04 cm (0.008 and 0.016 inch). The sands of the dunes are also well sorted and almost equal in size. Since quartz resists chemical weathering and is harder than most minerals, windblown sand in most cases is composed of quartz (Breed et al., 2019).

Winds

The three factors that are taken into account when talking about winds are – direction, velocity and turbulence. Since Earth moves west to east, the winds circulate in a clockwise direction in the Northern Hemisphere and a counterclockwise direction in the Southern Hemisphere in the subtropical areas of high atmospheric pressure (Augustyn et al., 2019) and that's where most of the great deserts are found (Breed et al., 2019).

The wind direction can also be altered by the obstructions in its path in the form of topographical features. It is interesting to note that the winds can also be channeled around

the dunes themselves, hence creating patterns of secondary wind flow that modifies the shapes of the dunes (Breed et al., 2019).

Wind velocity is an important factor too as it affects the amount of sand blown. The amount of sand moved by wind is a power function (exponential factor) of the wind speed (Bagnold, 1941). For example, a 10-km-per-hour wind carries 13 grams per hour, a 20-km-per-hour wind carries 274 grams per hour, and a 30-km-per-hour wind carries 1,179 grams per hour. The grain size also varies, a stronger wind will blow more of the larger grains than smaller grains. Also, strong winds often blow from a particular direction compared to lighter winds blowing from several different directions. As a result, sands which are finer in case of lighter winds are affected by several winds (Breed et al., 2019).

Bagnold formula can be expressed as:

$$q = C \frac{\rho}{g} \sqrt{\frac{d}{D}} u_*^3 \quad , \tag{1}$$

, where q represents the mass transport of sand across a lane of unit width; C is a dimensionless constant of order unity that depends on the sand sorting; ρ is the density of air; g is the local gravitational acceleration; d is the reference grain size for the sand; D is the nearly uniform grain size originally used in Bagnold's experiments (250 micrometres); and, finally, u_* is friction velocity proportional to the square root of the shear stress between the wind and the sheet of moving sand.

Formation and Growth of Dunes

A sand dune has 2 different sides called lee side (also called slip face as sand slips down this surface) and stoss side or stoss slope. The sides are named based on the paleo-current direction. As can be seen in Figure 6 below, the stoss side of the dune has a gradual dip and is on the side of the wind direction while the lee side (or slip face) is steeper in comparison due to the angle of repose.

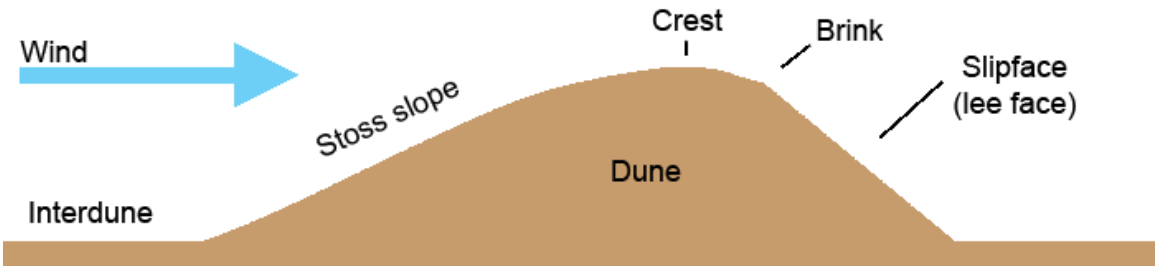

Figure 6: Lee and stoss faces of a sand dune with respect to the paleocurrent direction

The sand movement happens as a result of sand grains jumping along the surface, a process called saltation (Bagnold, 1941). The harder the surface, the easier the movement. As a result, more sand moves over a pebbly desert surface than over a smooth or soft one. Smooth surfaces reduce the amount of moved sand and a small patch of sand starts forming. A larger patch attracts even more sand (Breed et al., 2019).

As the wind hits this patch, the near-surface velocity decreases while depositing sand during this whole process over several metres, building up a dune. It is interesting to note that eventually the windward slope is adjusted leading to a re-increase in the near-

surface velocity up the slope. This velocity increase compensates for the drag force imposed by the sandy surface (Breed et al., 2019).

The gradual growth of the sand dune makes the smooth leeward slope more and more steep to the point wind cannot follow the sand sharply enough. This causes the formation of a "dead zone" which can be defined as a hollow surface formed as wind separates from the surface of the lee side. The sands coming up now from the stoss side fills up this hollowed surface. When enough sand is filled, such that the angle of repose of dry sand is about 32˚ (Figure 7), the sand starts slipping down again on the lee side and the equilibrium is achieved. This whole process keeps happening and consequentially the dune moves forward as a whole, sand eroded from windward face and deposited on the lee face.

Logically, the smaller dunes travel faster than bigger dunes. The three main reasons for this are – quantity of sand being more in bigger dunes, higher wind velocity required for bigger dunes and more cross-sectional area of bigger dunes. The first two factors are self-explanatory. As for the last factor, the smaller cross-sectional area requires less sand to be transported to reconstitute their form one dune-length downwind and achieve equilibrium. The movement speed of the dune varies from 20 metres per year to as fast as 100 metres per year (Breed et al., 2019).

Types of Dunes

The wind doesn't always blow in one constant direction. The wind is not a uniform stream and generally flow from different directions. As a result, sand dunes take different geometric shapes. Going from desert to desert, various types of dunes can be formed on

Earth, instances have also been seen on Mars (Malin et al., 2019) in the past. The average height of dunes is about 650 ft and the average spacing between the dunes varies from hundreds of feet to more than 1.25 miles (Breed et al., 2019).

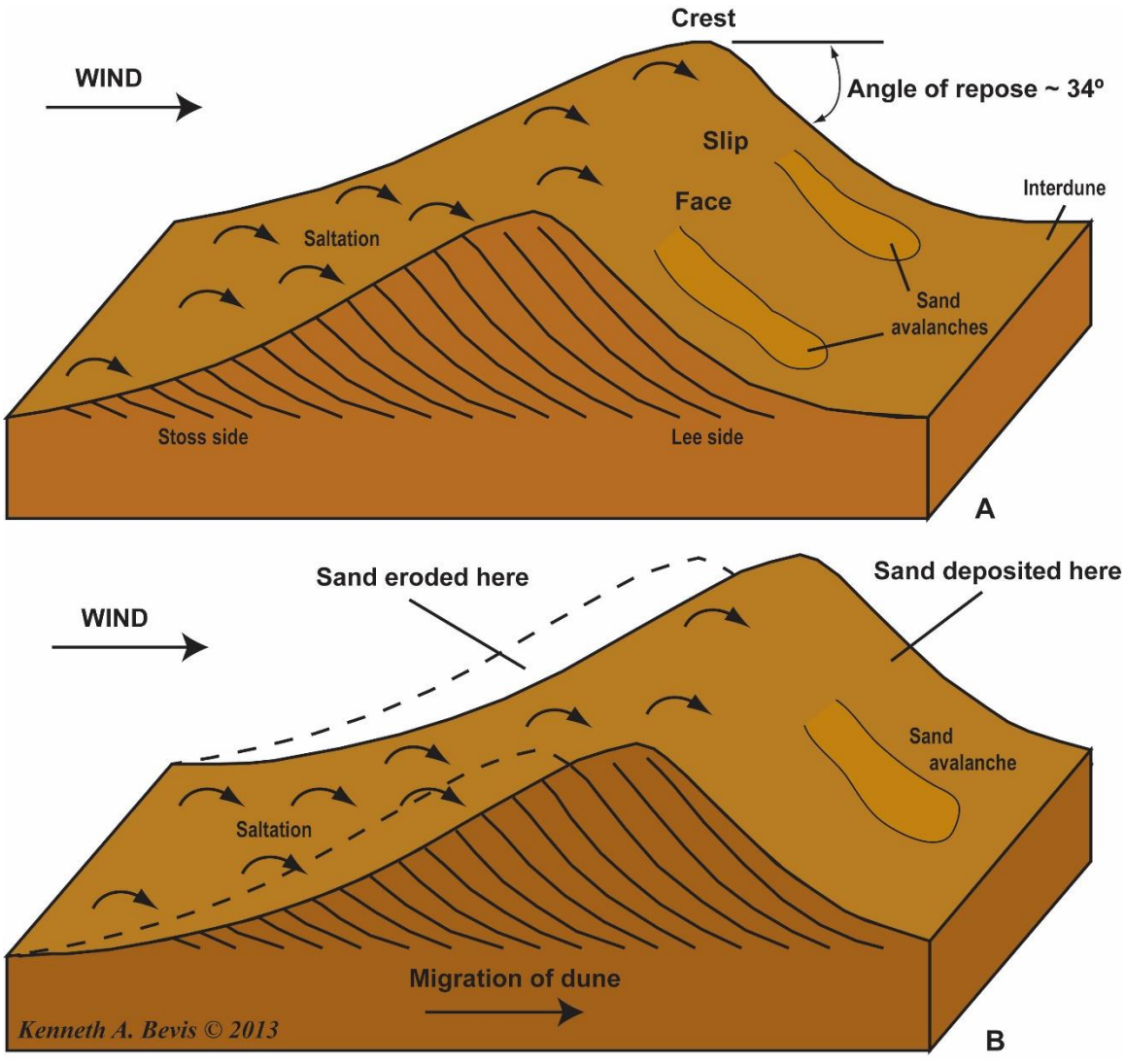

Figure 7: Formation and propagation of a sand dune (Bevis, 2013)

Based on the morphology of the sand dunes, they can be divided into five major types (Olsen, 2010).

1. *Barchan or Crescentic*

These are often referred to as the classic dunes as they are the most common types of sand dunes across the world. As can be seen in Figure 8, the barchan dunes resemble crescent-shaped sand bodies with convex backs and steep concave faces. The curved tips point downward and kind of enclose a single lee or slip face. These kind of dunes are formed in areas with unidirectional wind.

The crescentic shape is due to changes in the velocity of the wind. It is interesting to note that the regular repetition of the crescentic dune shapes indicates that the changes in the wind velocity are also regular. It is believed that the flow of a fluid arranges itself in long spiral vortices parallel to the flow direction, which, with zones of faster and slower velocities arranged traverse to the flow, gives a regular sinuous pattern on the bed (Breed et al., 2019).

2. *Parabolic or Blowout*

The parabolic dunes are very similar to the barchan dunes. The only difference is the direction of the tips. In case of barchan dunes, the tips point towards the lee or slip face while in case of parabolic dunes, the tips point into the wind or towards the stoss side. The main body of these dunes moves with the wind, hence the depression between the tips. Because of the same reason, they are also called blowout dunes. These types

of dunes are mostly formed around the vegetation which stabilizes the sediments and the U-shaped blowouts are contained between 2 clumps of plants.

*3. Transverse**

Contrary to the previous two types, the transverse dunes are linear in shape. They are formed perpendicular to the wind direction. The wind velocity associated with these dunes is lower than others and the quantity of sand is comparatively abundant. The single lee face of these dunes is generally steeper than other types of dunes. When present in groups, they resemble the appearance of sand ripples in large scale. Note that the * indicates that the sand dunes seen in this dataset and study are transverse dunes.

4. Linear or Longitudinal

Linear dunes are formed as a result of winds converging from at least two directions resulting in long ridges or lines. These dunes are formed in areas with abundance of sand. Since winds blow from both directions, both the surfaces of these dunes are called slip faces. The crests or dune tops are generally straight but sometimes can be slightly wavy in shape. It is interesting to know that the linear or longitudinal dunes can be as long as 62 miles.

5. Star or Pyramidal

Star dunes are formed when wind blows from multiple directions in areas of huge abundance of sand. These dunes have 3 or more slip faces and 3 or more sinuous ridges radiating out from a central sand peak, which makes them appear like a star. These

dunes are the only ones which do not migrate along the ground but instead grow vertically, hence called pyramidal. Because of this same fact, the star dunes are the largest and highest dunes. (Olsen, 2010)

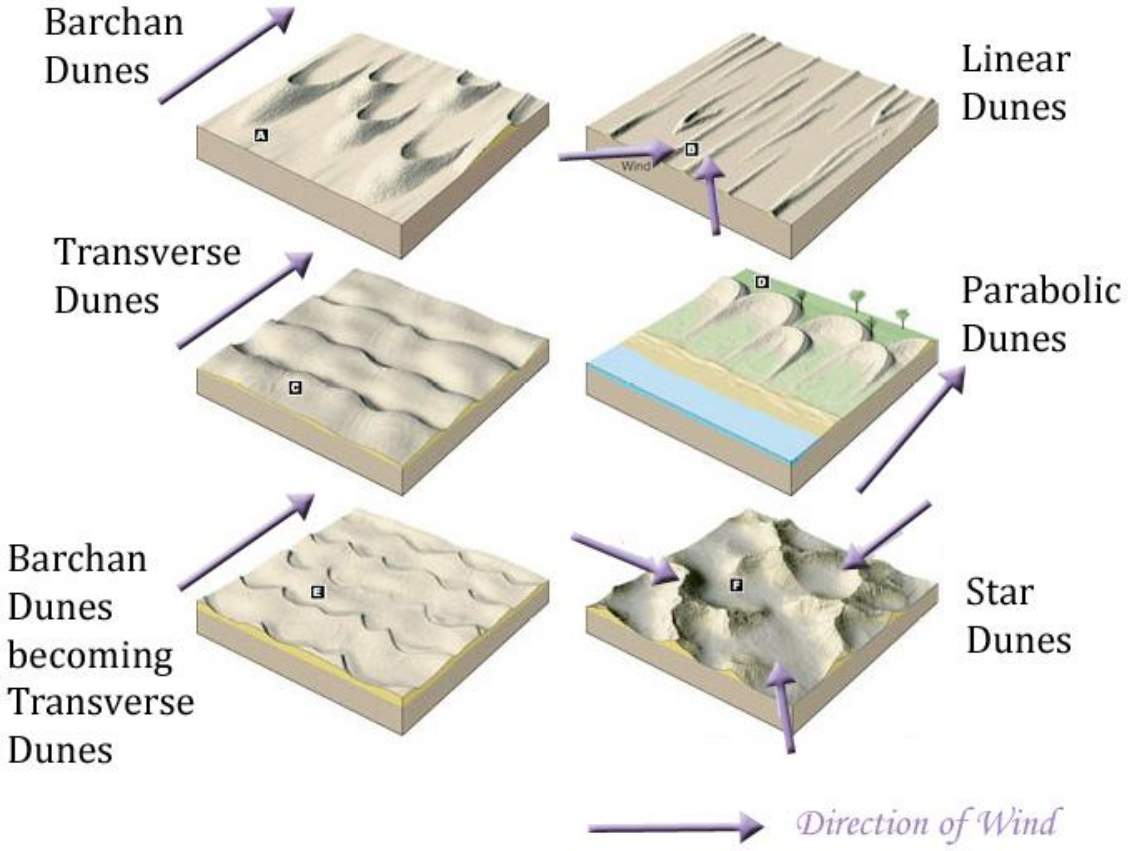

Figure 8: Major types of sand dunes

The sandy terrains occur in distinct sizes too. Large features are covered with smaller ones, and the smaller ones are covered with ripples. Based on the size of dunes and their occurrence with each other, all the five major dunes can be further categorized into simple, compound, and complex types.

When they occur in their original states, all dunes are simple. When a smaller dune forms on top of a larger dune of a similar type and orientation to the wind, the entire structure is known as a compound dune. When a smaller dune forms on top of a larger dune of a different type, it is known as a complex dune (Olsen, 2010).

The last thing that needs to be discussed associated with dunes is the water saturation. Prolonged drought conditions in the Navajo Nation (a Native American territory) has led to the reactivation of stabilized sand. This is because the vegetation in the area, which used to stabilize the sand, does not receive enough water to continue growing on the dunes. This is basically similar to deforestation where loss of vegetation leads to erosion and consequentially loose sands blowing around.

Additionally, it is very hard for plants to grow on sand dunes which keep on moving. Only a few species of plants can keep pace with moving sand dunes and tolerate the sands completely covering them continuously on the slip or lee face. Add this to the fact that sand itself is not a great source of nutrients for plants to grow in and as a result of loss of precipitation, the dunes themselves lose their inherent moisture which further aggravates the problem (Breed et al., 2019).

Figure 9 below shows an outcrop in the Arches National Park in Utah. The outcrops of the Navajo Sandstone can be seen in both the Arches National Park and the Canyonlands National Park, both located across each other in Moab, Utah. The picture clearly shows that the type of sand dunes here is transverse dunes. There are multiple cross beddings present here but they are all modern sand dunes subjected to erosion in the past. Because

of the erosion and the picture taken from the top and not of the cross section, it is hard to determine the wind direction with confidence. The picture was taken after noon, the sun rises in the east and sets in the west. The casted shadow is pointing towards the east, which makes the direction from right to left same as NW to SE. To measure the accurate wind direction, strike and dip of the individual dunes must be measured and averaged.

The visit to the Arches National Park had dual purposes. The first was to try to confirm the dominant wind direction of the Navajo Sandstone in the Arches National Park which was not possible because of dunes being eroded. The second and more important reason of the visit was to understand how the sand dunes actually look in outcrops and to understand the ease of determining the dominant wind direction even when the main sand dunes are surrounded by minor cross beddings. However, if one is trying to study the height of the sand dunes, Canyonlands National Park is a better place to go since the dunes there match the height of the average of 200 ft.

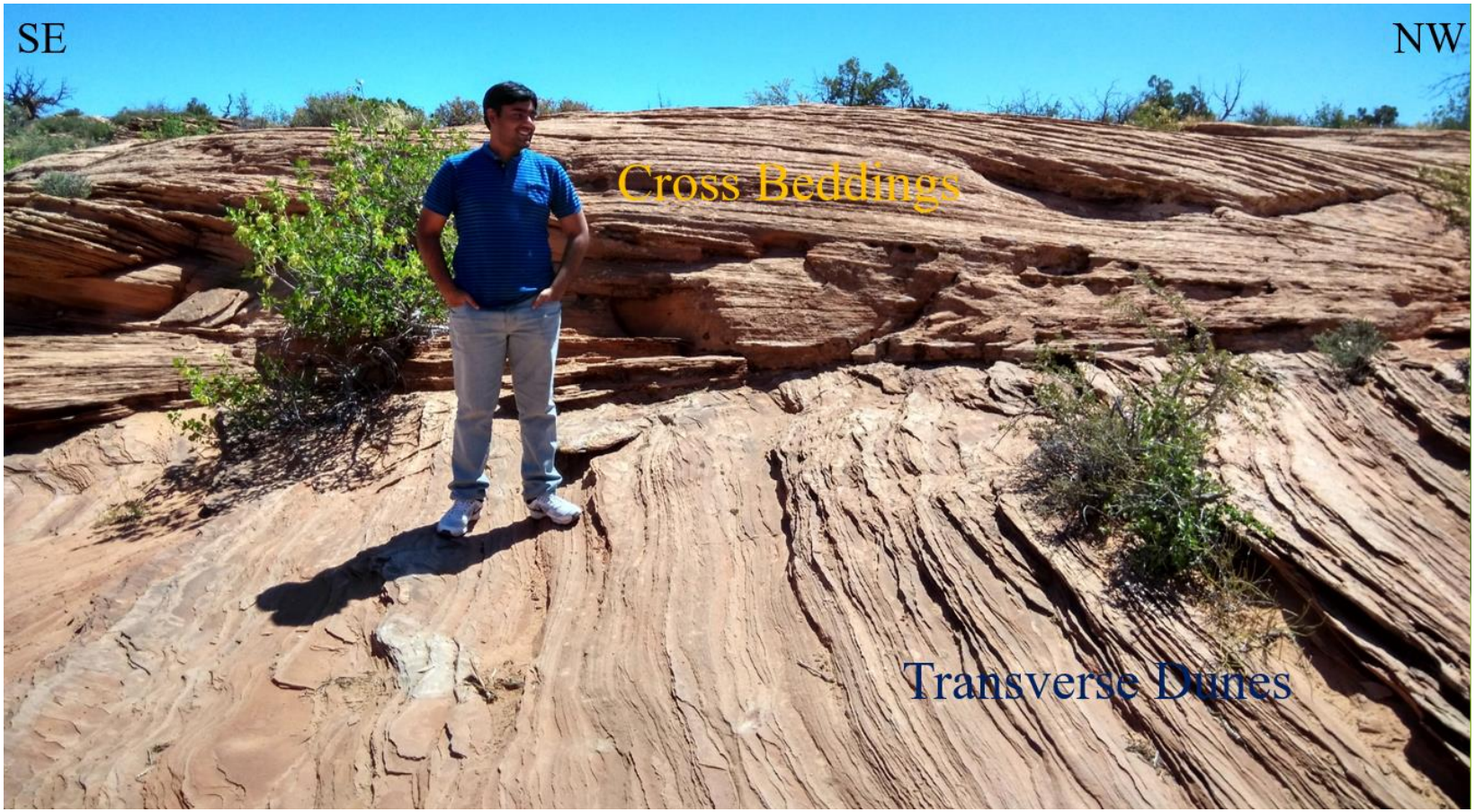

Figure 9: An outcrop in the Arches National Park which shows the cross beddings of the modern sand dunes (subjected to erosion) from the Navajo Sandstone of Utah

CHAPTER 5

SEISMIC AND WELL LOG DATA ANALYSIS

A 3D seismic survey of about 36 mi^2 area along with 3 well logs surrounding the survey were used for this research. A, B and C are the three wells. The other wells are not deep enough to penetrate the interesting features studied in this research and hence were not used. Well A is located about 3 miles to the northeast of the survey and the wells B and C are present about 4.5 miles to the southeast of the 3D seismic survey (Figure 3). The seismic survey was acquired with a dynamite source and a 5 sec record length, with a maximum offset range of 14,500 ft in 1999.

The low dip and continuity of the later Paleozoic (deeper) and the Mesozoic (shallower) formations, without a large-scale heterogeneity, allows the use of the above-mentioned wells for the well to seismic tie (Figure 11).

Triple combo logs were used to perform basic and advanced petrophysical analyses of the Nugget Sandstone. Common well log patterns and cross-plots helped in identifying general lithology, fluid content, and estimating fluid saturation. The Nugget Sandstone was identified as an overall sandstone formation based on its low gamma signature and because the density porosity values are higher than neutron porosity. The formation also shows occasional peaks in the gamma ray (GR) curve (Figures 10B and 11), which can be attributed to the presence of clay. Different cross-plots including sonic-bulk density and Pickett plot were produced to have a deeper understanding of the lithology and computing fluid saturation (Figures 10A and 10B). Sonic-bulk density crossplot color-coded by PE

(photoelectric) log (Figure 10A) revealed the presence of minerals with very low density (<2.2 g/cc), high photoelectric values, and relatively higher velocity than the majority of the samples (Verma et al., 2018). This pattern is indicative of a few minerals in the evaporites group (e.g. halite and sylvite) commonly present in sand dunes. In the next step, a Pickett plot (Figure 10B) was generated to identify fluid type and derive required parameters for Archie-based water saturation estimation (Archie, 1942).

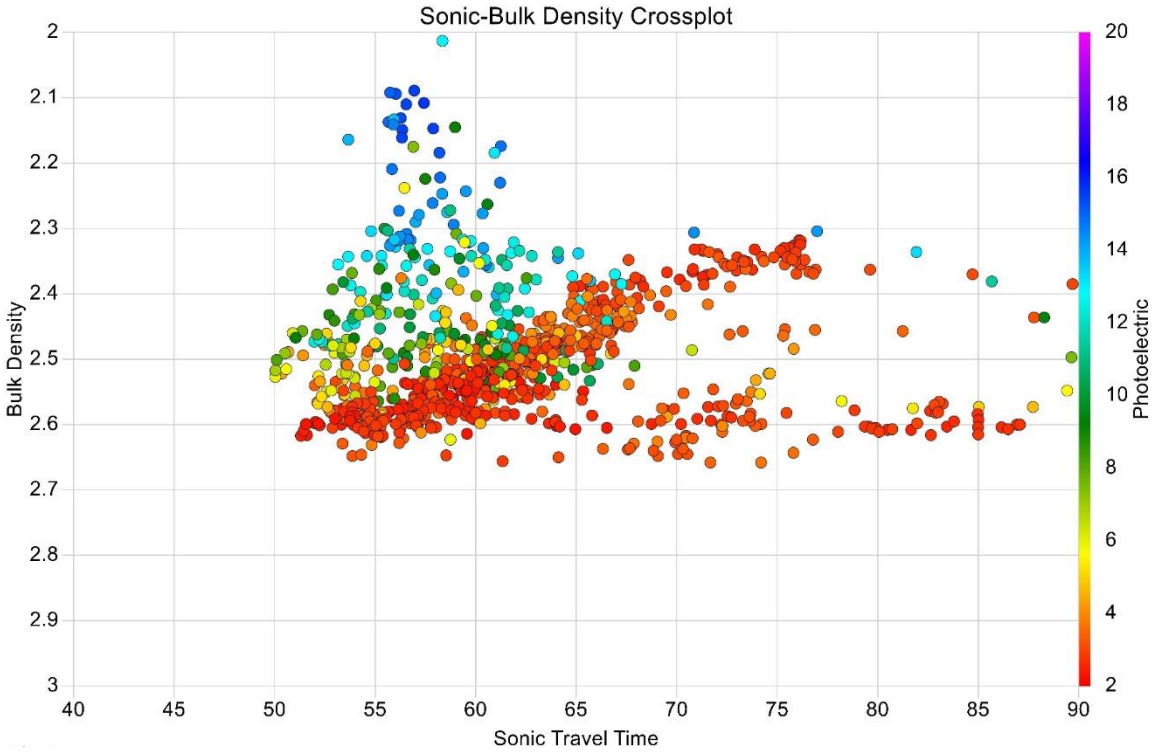

Figure 10: A) Sonic-bulk density crossplot color-coded by photo-electric curve shows heterogeneities present in the Nugget Sandstone (Verma et al., 2018)

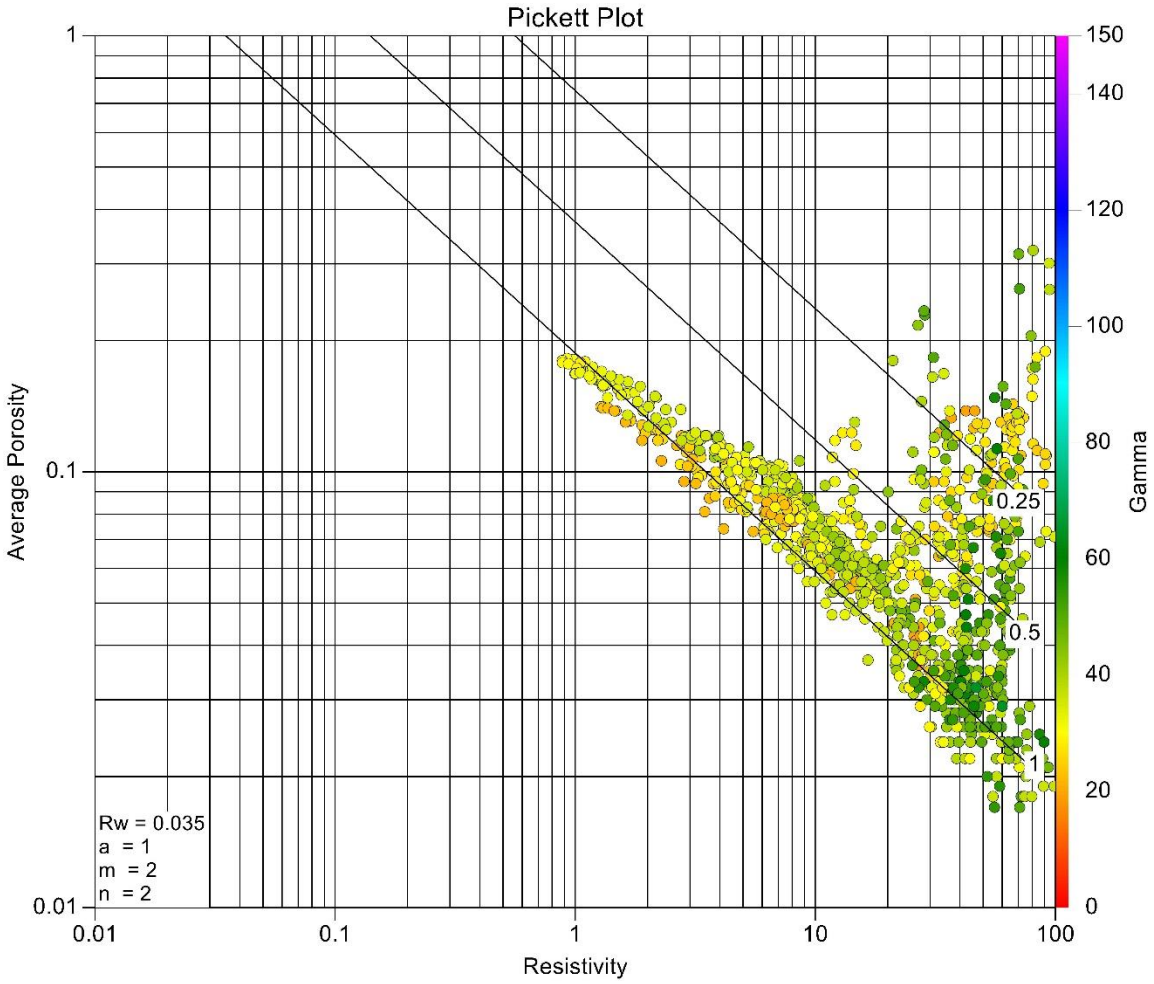

Figure 10: B) Pickett plot color-coded by gamma-ray curve showing lines at different water saturation of 100%, 50%, and 25% in the Nugget Sandstone. The parameters used in the Archie equation for water saturation calculation are written in figure (Verma et al., 2018).

A Pickett plot is a graphical technique that plots resistivity and average porosity (computed from neutron and density porosity) values on a log-log scale to determine water saturation using Archie's law. Archie's equations can be expressed as (equation 2):

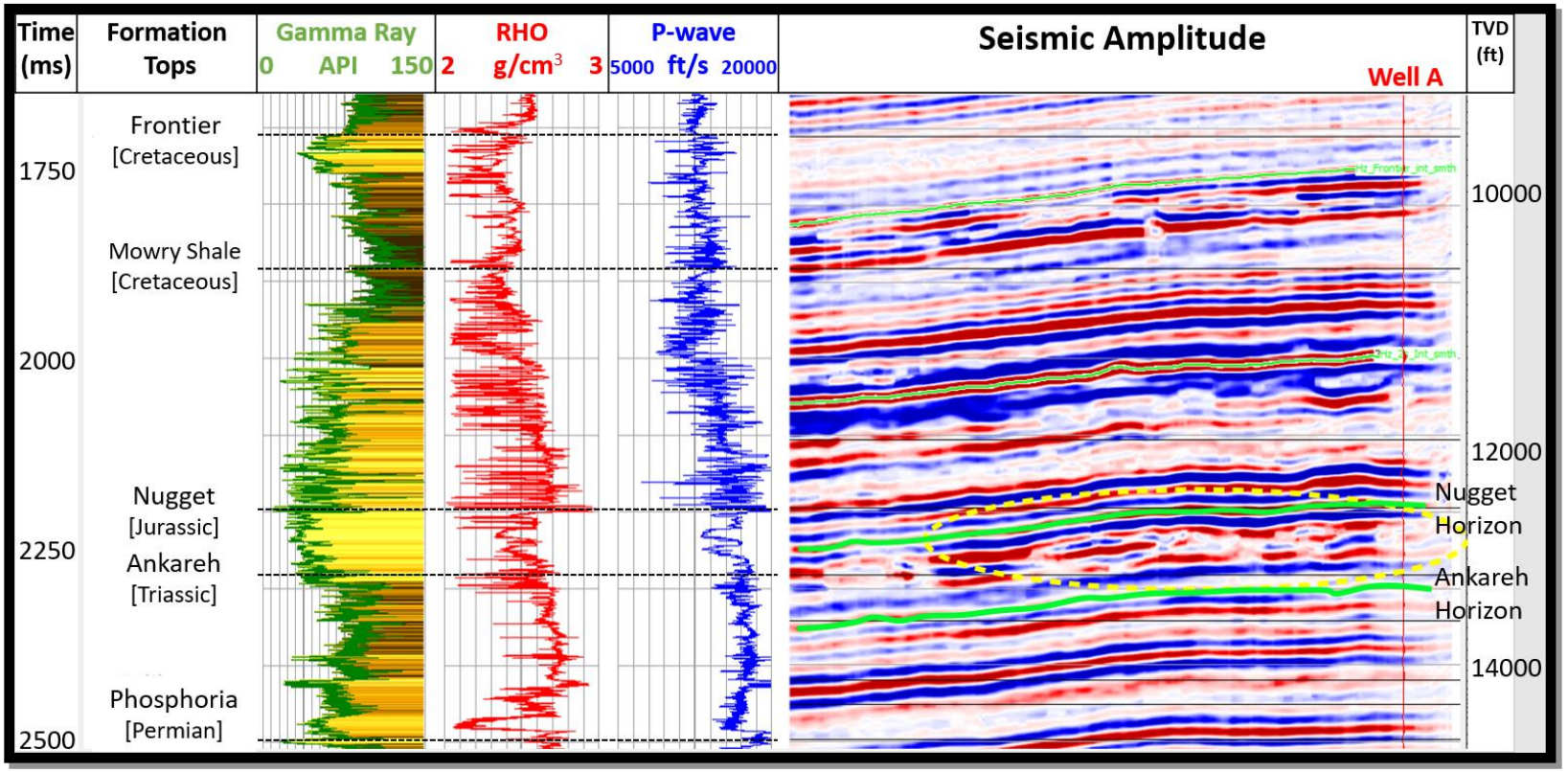

Figure 11: Well to seismic tie – Well A. Well A highlighted as red vertical line. The yellow ellipse exhibits the structures of interest.

$$\frac{R_t S_w^n}{R_w} = \frac{a}{\phi^m} \quad , \tag{2}$$

, where ϕ = porosity; S_w = water saturation; a = proportionality constant varying from 0.6 to 1.5 (tortuosity); m = cementation factor that varies between 1.3 and 3; n = saturation exponent, often assumed to be 2; R_w = resistivity of the formation water; and, R_t = true resistivity of the formation. Note that if S_w and ϕ are equal to 1, R_t equals the product of a and R_w (SEG, 2019).

The plot showed that most of the samples from the Nugget Sandstone are water-bearing. The slope of the constructed lines at different water saturation (100%, 50%, and 25%) can be used to determine the values of cementation factor (m) as needed in the Archie equation (Rider and Kennedy, 2011). The values of a, m, n, and R_w in the Archie equation were 2, 2, 1, and 0.035 ohm-m, respectively (Verma et al., 2018).

Petrophysical inversion was performed and statistical multi-mineralogical solutions for wells C and A were obtained, using commonly utilized well logs (Savre, 1963; Moss and Harrison, 1985; Mitchell and Nelson, 1988; Kulyapin and Sokolova, 2014). This inversion helped in better understanding the mineralogical composition and facies variability in the Nugget Sandstone at well-log scale. Mudlogs available in the wells were used to augment the quality of petrophysical inversion based multi-mineralogical solution. Input well logs selected for the statistical multi-mineralogical solutions were gamma, neutron-porosity, bulk density, and Umaa. Umaa is the product of photoelectric and density log corrected by apparent total porosity. Calculated output curves are the volumetric

proportions of quartz, illite, kaolinite, calcite, dolomite, anhydrite, halite, gypsum, and bulk volume water (Figure 12). Standard values of gamma, neutron porosity, bulk density, and Umaa logs for each mineral were used to generate corresponding synthetic logs. Synthetic logs at different mineralogical proportions were compared to the actual well log response from the Nugget interval. The mineral type, parameters, and number of iterations were optimized to obtain the precise multi-mineral solution with minimum error (< 2%). The error was computed from the difference of synthetic log and actual well log.

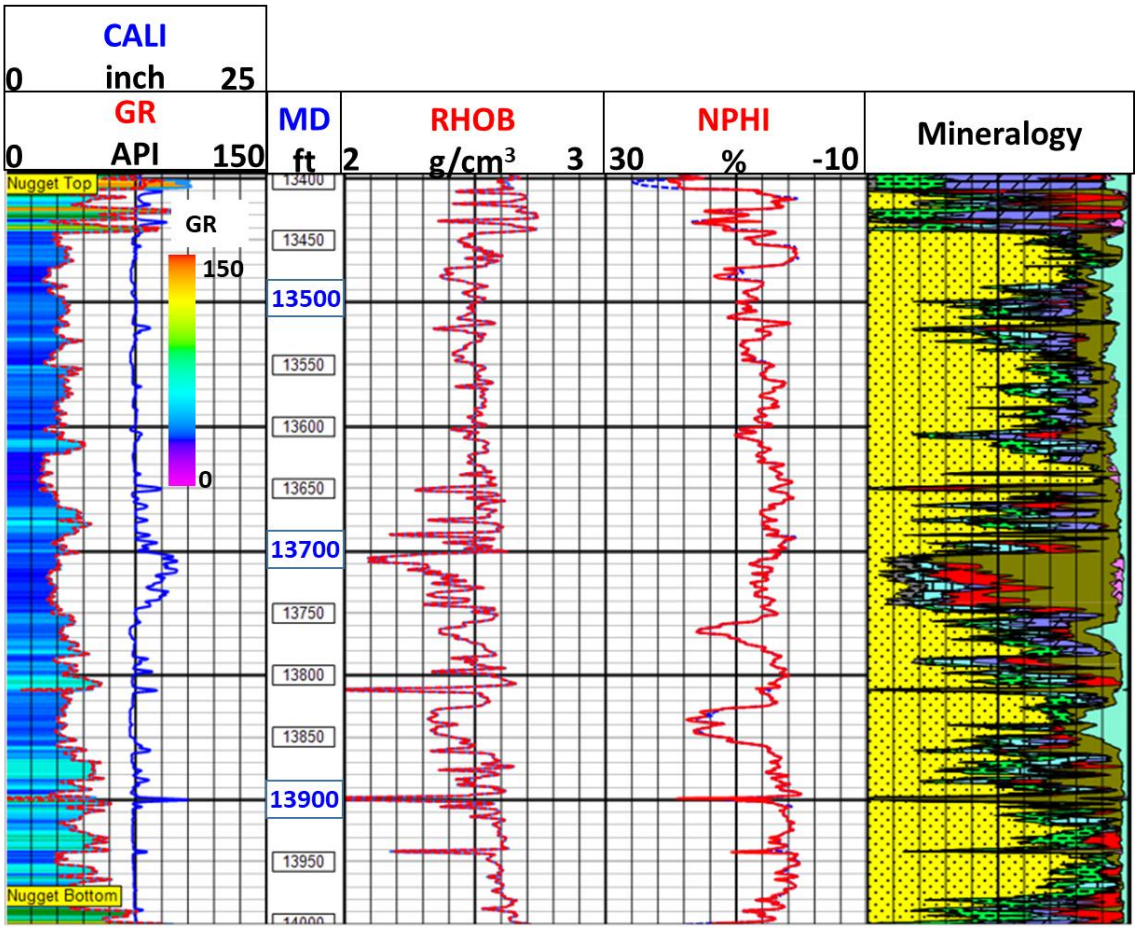

Figure 12: A stochastic mineral solution from the well C showing actual and synthetic well logs (marked by R). The first three tracks show the common well logs – gamma ray,

bulk density and neutron porosity. The fourth track shows the multi-mineralogical solution. The overlapping pattern of all synthetic logs on the actual well logs indicates significantly less error in inversion. The Nugget Sandstone formation is composed of multiple minerals in different proportions, including quartz, illite, kaolinite, calcite, dolomite, anhydrite, halite, gypsum, and water (Verma et al., 2018).

The statistical mineral solution reveals that the Nugget Sandstone is complex, and it is composed of various minerals that cannot be visualized easily with basic well log analysis techniques. Although the formation is mostly composed of quartz (> 50-60%), it contains clay, carbonate, halite, anhydrite, and gypsum in variable proportions. An anhydrite bed is present near the top of the Nugget Sandstone formation in both wells. A thick halite-anhydrite bed is present in the middle of the Nugget Sandstone formation in the well C. Halite is more abundant than anhydrite and gypsum (Verma et al., 2018).

Also, the same mineral solution for the well A shows a slightly different composition. The Nugget Sandstone is still primarily sands, but well A showed more evaporites than sands (Figure 13). This informs about the lithological heterogeneity present within the Nugget Sandstone in the survey area. Note that the formation thickness remains ~500 ft throughout the seismic survey (going from well A at the top to well C at the bottom).

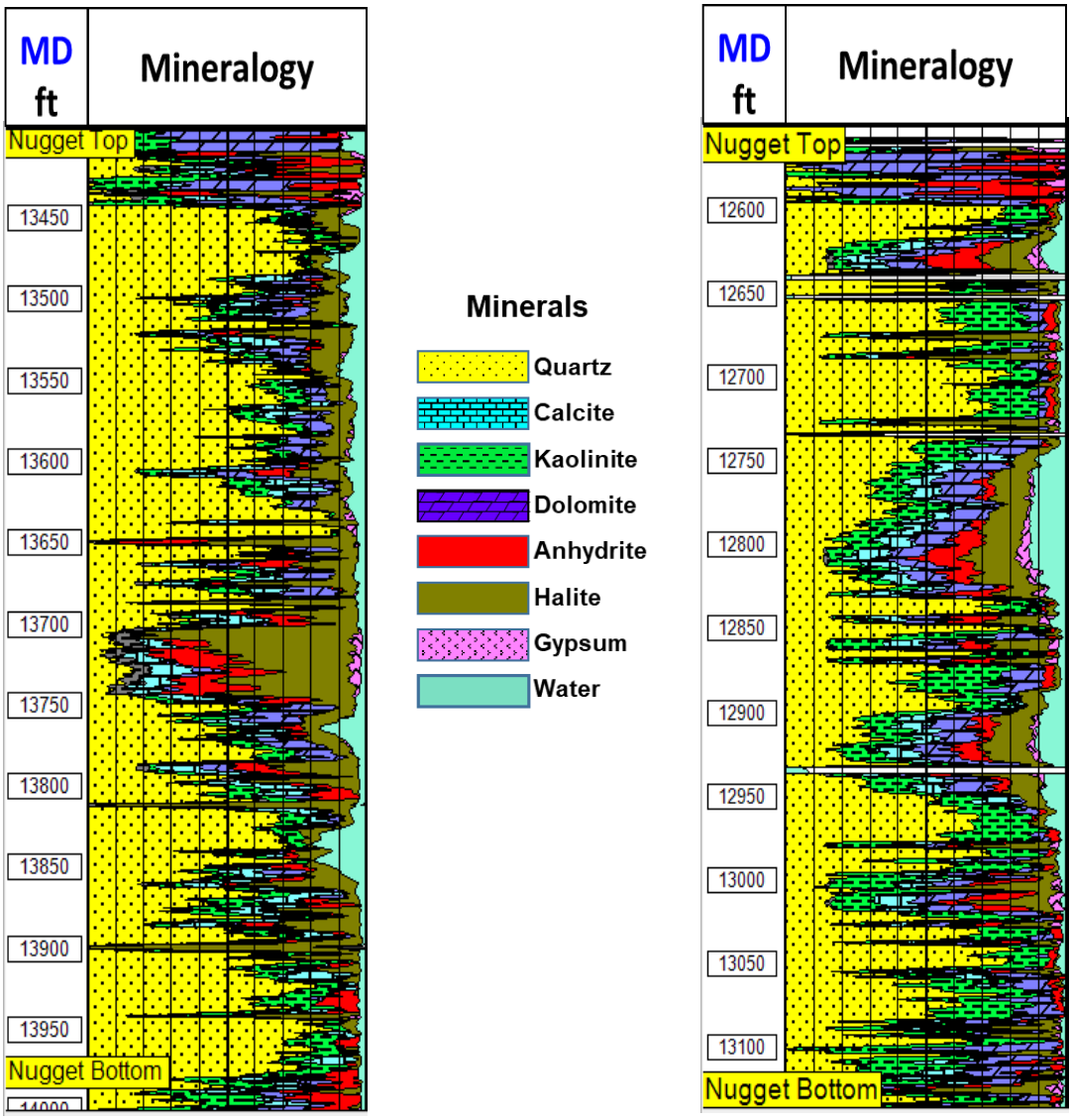

Figure 13: Statistical multi-mineralogical solutions for the wells C and A. Although the solutions indicate the Nugget Formation is predominantly sandstone, there is a significant amount of internal heterogeneity present. Based on our analysis, it appears that the well C is more representative of a sand dunal environment, whereas the well A suggests more of an interdunal environment (Verma et al., 2018).

Seismic Attributes

A seismic attribute can be defined as a quantity extracted or derived from seismic data that can be analyzed in order to enhance information that might be more subtle in a traditional seismic image, leading to a better geological or geophysical interpretation of the data (Schlumberger, 2019). The most basic seismic attributes that one can think of are the measured time, amplitude, frequency and attenuation. The more complex seismic attributes, which are now being used in the exploration industry, are combinations of two or more of these basic attributes. Seismic attributes are generally calculated on the post-stack seismic data. The very first attributes that were developed and practically used were envelope amplitude, instantaneous phase, instantaneous frequency etc. Acoustic impedance obtained as a result of seismic inversion can also be considered an attribute and was among the first ones to be used for interpretation (Sheriff, 2002).

Based on the features an interpreter is interested in, the signal and noise of the seismic data can be interchangeably used for the calculation of various seismic attributes. Chaos and ambient noise are some examples of noise attributes among others. There can be as many seismic attributes as the stars in the sky. The attributes associated with dip are dip components, dip magnitude, dip azimuth, dip confidence, etc. New attributes can be calculated by squaring or cubing or taking the first or second or further derivatives of a single seismic attribute. For example, if an interesting feature in seismic data is not resolvable or is unnoticeable in a linear attribute, it will be more evident and clearer in the square or cube of the same attribute. So, to delineate the seismic features, mathematical operations are performed on the basic attributes.

For the purpose of this research, 3 main attributes were used which are similarity (coherence), curvature, and acoustic impedance. Attributes can be directly used on seismic data to concentrate on the structural features. However, in some cases, the attributes are used on the flattened seismic section on a picked horizon. When the seismic data is flattened with respect to a horizon, the layers below and above the horizon are rearranged such that the horizon in case is completely flat. This is done in order to focus on the stratigraphic traps rather than the structural traps. Since sand dunes were deposited in Early Jurassic age, the best way to see the effect of the deposition is by looking at stratigraphic slices and therefore all the attributes discussed below were used on the flattened seismic section with respect to the top horizon of the Nugget Sandstone which contains all the features of interest.

Similarity (Sobel filter or Coherence)

Similarity is an edge detection attribute and one of the most common seismic attribute used to identify faults, channels or other discontinuous features on a surface. It detects the break in reflector configuration or lateral changes in amplitude values and waveform shape (Qi et al., 2017) and is used to map the lateral extent of a formation. It represents the similarity or continuity between two points. If two neighboring points are similar or continuous to each other, then coherence is 1, if they're completely dissimilar then the value of coherence is 0 (Agrawal et al., 2018). Since the depth and thickness of a sand dune structure is different from an otherwise flat interdune, the sobel filter attribute proved to be very useful in demarcating the size and extent of the sand dunes and interdunes.

Like any other attribute, similarity can be expressed in terms of various different attributes which are better in one case or another to each other. A few types of similarity attributes are energy ratio similarity, outer product similarity, sobel filter similarity, gradient components, total energy, coherent energy, etc. The primary attribute used in this research is sobel filter or coherence. The arrows in Figure 14 below shows various dune and interdune structures.

The sand dunes, in the Figures 14, 15, and 16 below, range in length from about 0.5 mile to about 3 miles. The thickness of these dunes can be identified by looking at these peculiar features in the seismic and converting the two-way time to depth based on the relationship obtained from the well to seismic tie (Figure 11). Figure 14B shows that the eolian dune lineaments begin to become prominent around 44ms. Note the blue arrow indicates the inter-dunal environment whereas the yellow arrow indicates the well-developed sand dunes.

Structural Curvature

The second most important attribute that was used to understand the peculiar features in question is the structural curvature. Mathematically, the structural curvature equals the rate of change in the dip of a surface. The first derivative of the dip is calculated in both the inline and crossline directions. If the dip continues to increase, for example in case of an anticline, the curvature will be positive. Similarly, a continuous decrease in the surface dip, like in a syncline, leads to negative curvature and a constant dip (flat surface) denotes 0 curvature. The curvature is used to represent the shape of the surface. Every

single point on a 3D surface has two principal curvatures denoted by k_1 and k_2 which are called the maximum and minimum values of the curvature respectively (Agrawal et al., 2018).

It is important to note that the shapes represented by different curvature values depend on the wavelength of the data one wants to look at. A syncline for small wavelength can be a part of a bigger anticline (longer wavelength; Agrawal et al., 2018). The combination of k_1 and k_2 may represent different shapes of the surface like dome, valley, ridge or bowl etc., (Roberts, 2001; Bergbauer et al., 2003; Al-Dossary and Marfurt, 2006). The mean curvature is calculated by averaging k_1 and k_2.

Like other attributes, curvature can also be expressed in terms of various other attributes based on the interpreter's requirements. A few examples of the curvature attributes are principal curvatures ($k_1 >= k_2$), strike of the principal curvatures (psi_1 and psi_2), reflector rotation about the normal, reflector convergence, 2D curvature amongst others. The shape measurements can also be expressed as a function of the principal curvatures. Some examples are curvedness, shape index, dome curvature attribute, ridge curvature attribute, saddle curvature attribute, valley curvature attribute and bowl curvature attribute and so on.

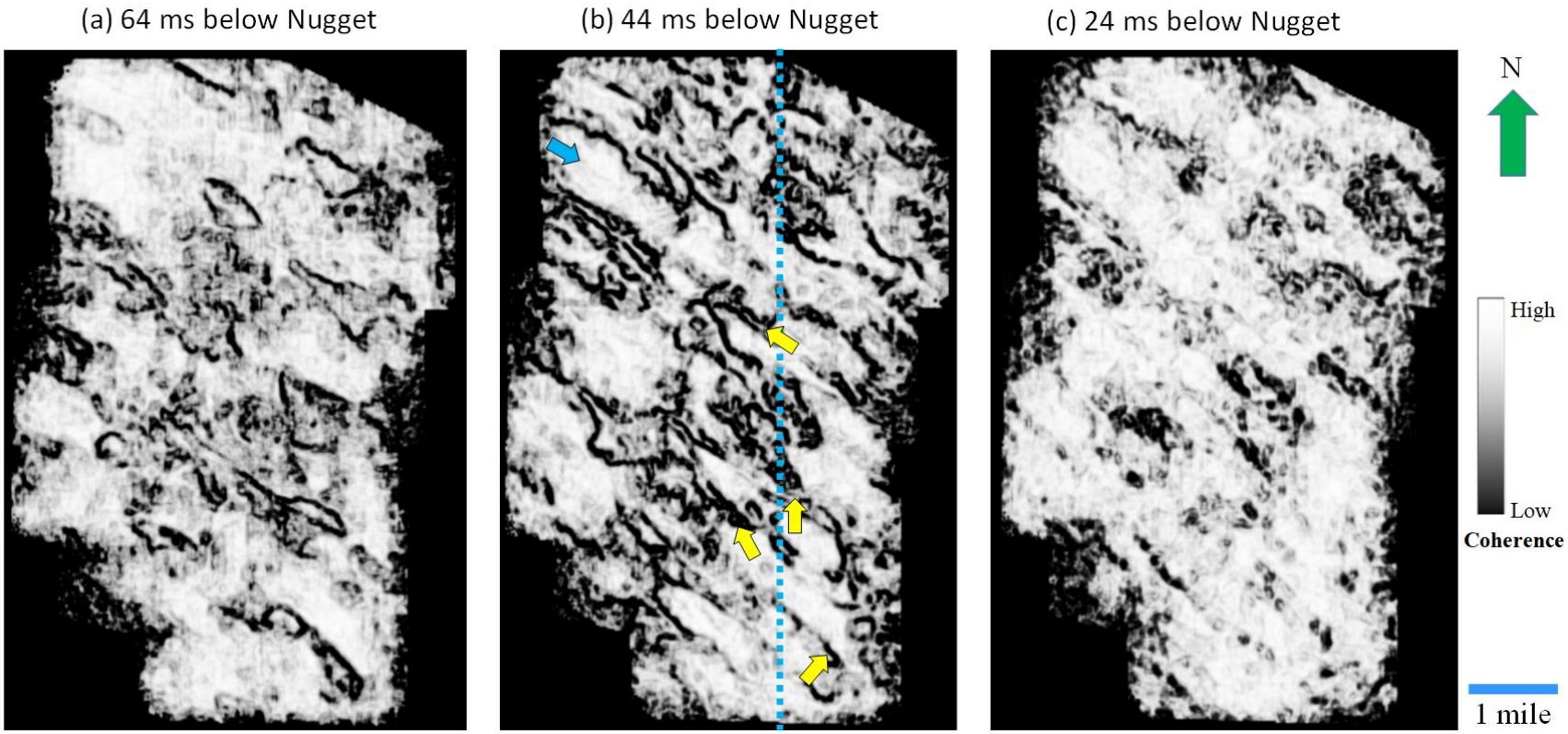

Figure 14: Stratal slices of the coherence attribute, 1 represents maximum similarity and 0 represents maximum dissimilarity. The eolian dune lineaments begin to appear 24 ms below Nugget (c), become prominent around 44 ms (b), and then start disappearing about 64 ms below Nugget (a). Note the blue arrow indicates the inter-dunal whereas the yellow arrow indicates the well-developed sand dunes.

The principal curvatures k_1 and k_2 have been used in this research. By looking at k_1 and k_2 co-rendered with the sobel filter (coherence) attribute, the presence of anticlinal and synclinal features on the stratal seismic slices was confirmed (Chopra and Marfurt, 2010). Presence of positive curvature k_1 inside the discontinuities evident from the coherence attribute indicates an anticline and the negative curvature k_2 along the discontinuities on both sides indicates synclines (Figure 15). So, the overall geology seems to be an antiform surrounded by synforms on both sides. The anticline in this case is a sand dune and the flat subsurface that occurs after the synclines and between the 2 consecutive sand dunes are the interdunal features.

GLCM Homogeneity

GLCM stands for gray-level co-occurrence matrix. It is a texture seismic attribute. In general, texture can be defined as a feel of a surface. It is expressed in terms of whether a surface is smooth or rough and the extent of it. When a texture is rough to the touch, the surface exhibits sharp differences in elevation within the space of the fingertip (AASPI, 2019). Similarly, a silky texture exhibits very small differences in elevation.

A few examples of the GLCM attributes are GLCM homogeneity, GLCM energy, GLCM contrast, GLCM dissimilarity, GLCM entropy, GLCM mean and GLCM variance. Figure 16 shows the GLCM homogeneity attribute, note how texture of the surface can be visualized in a way that the stoss and lee side of the dunes are illuminated significantly.

The gray-level co-occurrence matrices are computed along structural dip. The output attributes provide images that are somewhat fuzzy and not very useful for human

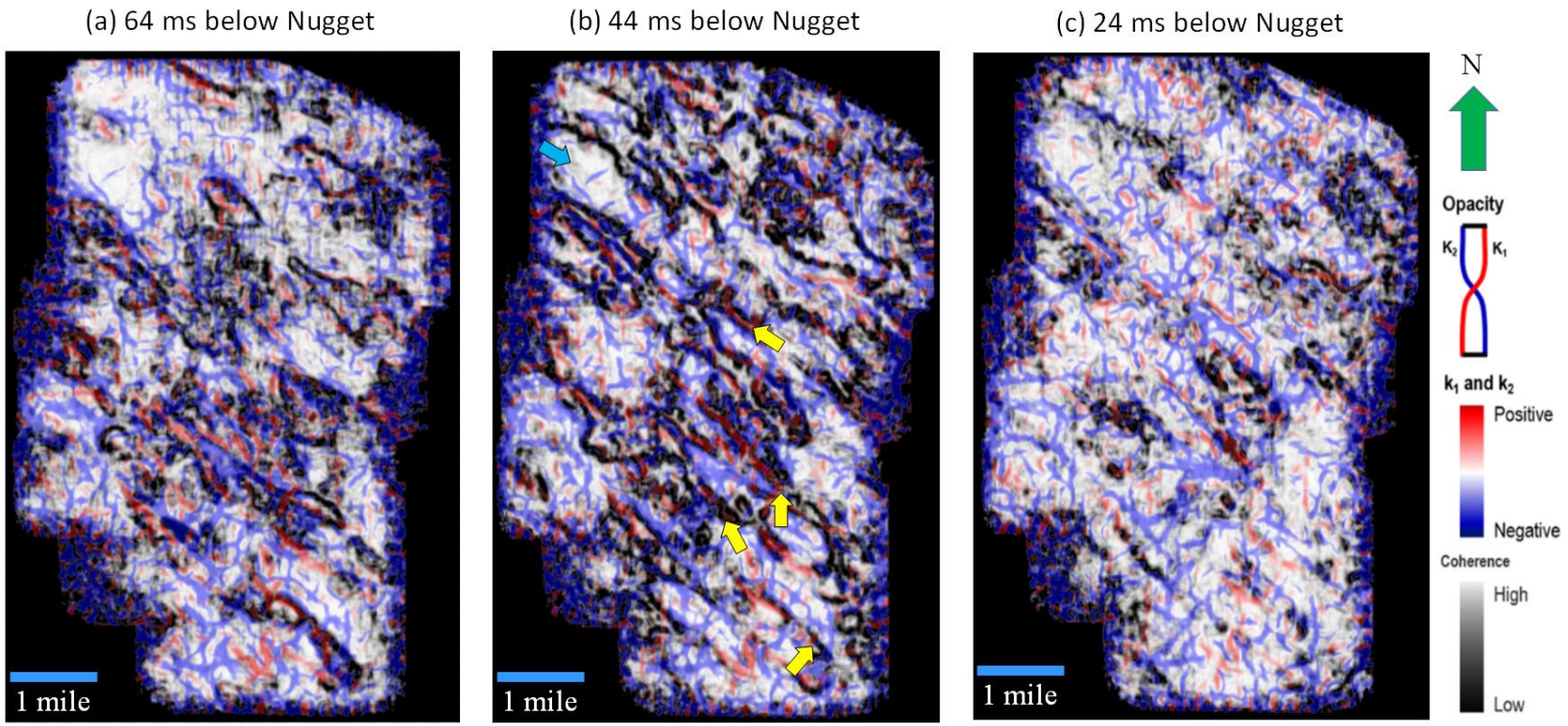

Figure 15: Stratal slices of most positive curvature (k_1), co-rendered with most negative curvature (k_2) and coherence. All slices are taken with respect to the Nugget Sandstone reflector. The eolian dune lineaments begin to appear 24 ms below Nugget (c), become prominent around 44 ms (b), and then start disappearing about 64 ms below Nugget (a).

interpretation. But these attributes serve as input data to self-organized maps, generative topological maps, or other clustering algorithms (AASPI, 2019).

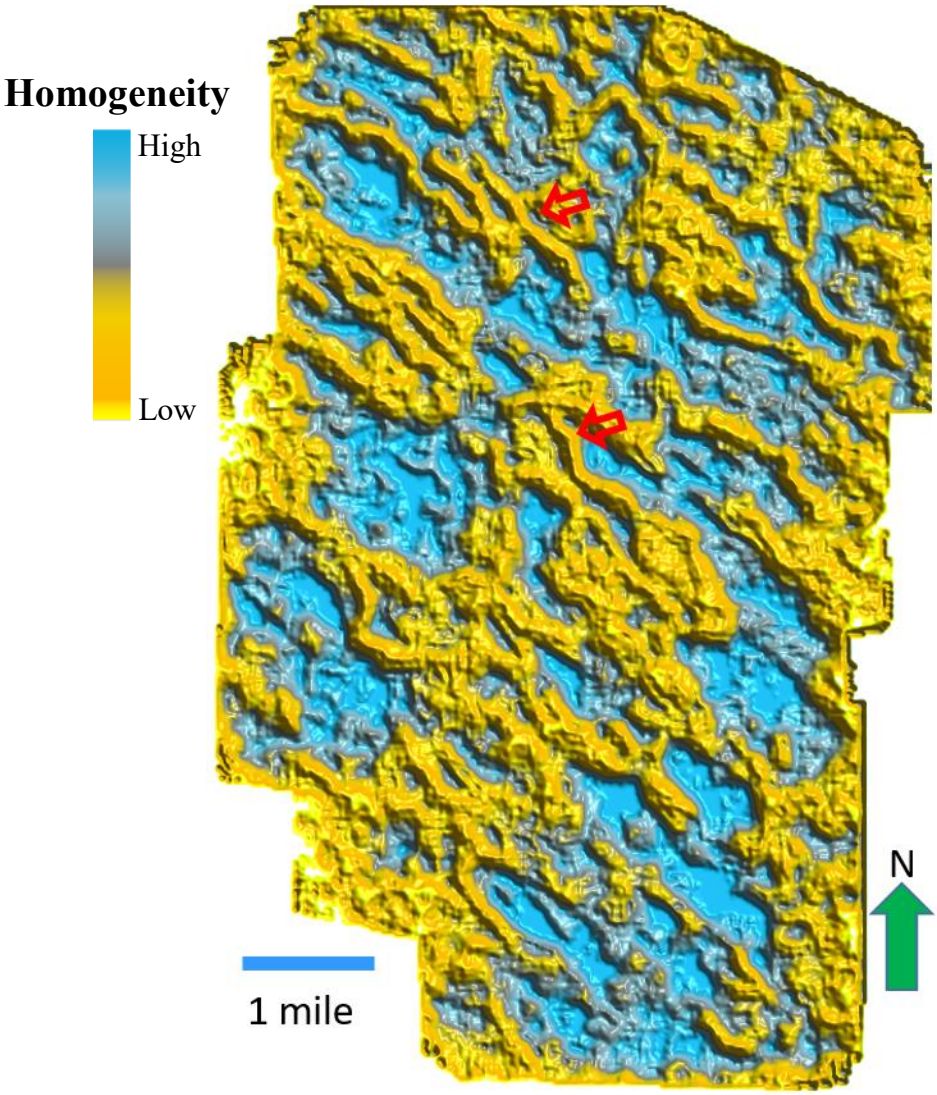

Figure 16: GLCM Homogeneity applied with a bump map (the red arrows illuminate the stoss side of the dunes with gradual dip)

Bump Mapping

Bump mapping is a technique which has been traditionally used in computer graphics. It helps simulate bumps and wrinkles on the surface of an object. This is achieved by altering or modifying the normal of the surface and using the new normal during lighting calculations. The output is an apparently bumpy surface rather than a smooth surface which looks more realistic. Bump mapping was introduced by James Blinn in 1978 (Blinn, 1978). It is important to note here that only the surface normal is modified and not the surface geometry itself. Because of this, although the surface of the underlying object remains unchanged, the final result looks like a bumpy detailed surface instead of a smooth surface. Bump mapping is also much faster compared to the actual displacement mapping because geometry remains unchanged. An example is a smooth sphere drawn in everyday mathematical calculation and an orange from real life (Figure 17).

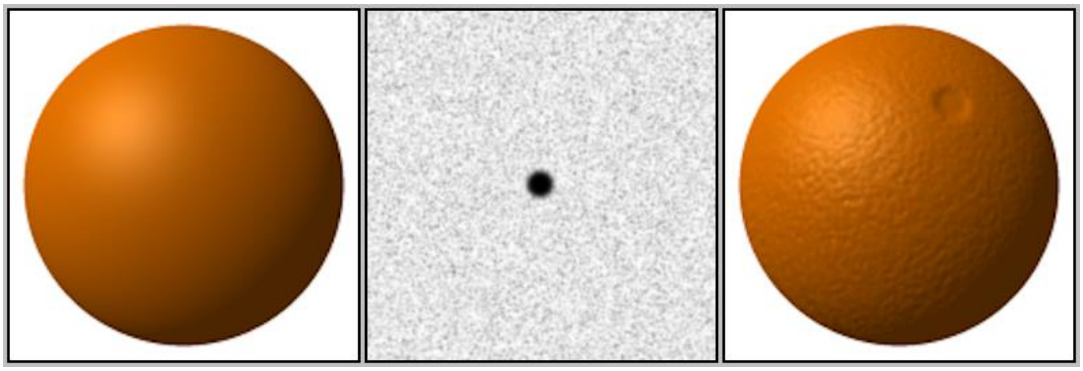

Figure 17: Left – sphere without bump mapping, Middle - bump map to be applied to the sphere, Right – sphere with bump mapping. Notice how the big black dot appears as the big bump on the right while other smaller dots generate smaller bumps. This is achieved

by changing how an illuminated surface reacts to light, without modifying the size or shape of the surface (GDallimore, 2010).

Now that the bump mapping concept is clear, it is easy to understand how Figure 16 demonstrates realistic sand dunes and interdunes that may have existed during Early Jurassic age. The bump map along with GLCM homogeneity resolves the finer parts of all the dunes and hence reveal the lee and stoss side of the dunes. The dunal areas with bumps, elevations and low GLCM homogeneity were colored yellow while the interdunal areas which appeared flat and high GLCM homogeneity were colored blue. Going from NE to SW, the structures appear to have a gradual dip until the sand dune top is reached and then steep dip until the flat interdune. By looking at various sand dune types explained in Chapter IV, it appears that the dunes in question are transverse dunes with wind blowing from NE to SW.

P-Impedance

Seismic waves can be divided mainly into two types – surface waves and body waves. As the names suggest, the surface waves move along the Earth's surface and are slowest in speed. These are the waves that make the ground roll up and down or shake it from side to side and cause the most damage to Earth. These are the waves that are primarily involved in destruction from an earthquake. The surface waves can be further expressed in terms of Rayleigh waves (R waves) and Love waves (L waves).

For exploration purposes, the body waves are used. The body waves are mainly of two types – primary waves (P waves) and secondary or shear waves (S waves). The P wave

is the fastest seismic wave with an average speed of about 3 miles per second and can travel in all mediums. The S waves are the second fastest with an average speed of half of that of P-waves. But unlike P-waves, the S-waves cannot travel through fluids (liquids and gases).

The seismic amplitude in the post stack data set is a quick and easy way to look at stratigraphic features without calculating tedious attributes and is generally comprised of mainly P-waves. The seismic amplitude indicates the points of change in impedance. P-impedance (often referred to as acoustic impedance, because P-waves are similar to sound waves) can be mathematically defined as the product of velocity of the P-wave and the density of the rock layer. The velocity of P-wave changes depending on what kind of medium it passes through. Generally, the denser layers allow a faster movement of P-waves. So the P-waves velocity varies from 1,080 ft/s in air to 4,600 ft/s in water to more than 16,000 ft/s in the crust of the Earth.

Seismic amplitude is a good option to identify impedance changes but it does not determine the actual value of impedance. To find the actual P-impedance, seismic inversion is done after the well to seismic tie which gives a velocity-density function. The values of impedances are very useful not only to identify the exact extent of the layers with similar lithology but also to determine the actual lithology of it. Since P-impedance helps in determining certain aspects of lithology from seismic data, it is also considered as a seismic attribute.

An example is that sands have low impedance value of about 30,000 (ft/s)*(g/cc) while evaporites have higher acoustic impedance value of about 50,000 (ft/s)*(g/cc). By

looking at the P-impedance curve on the time slice (Z slice), one can focus on the changes of sand lithology to evaporite lithology and also be able to tell how drastic or mild the changes are from one subsurface point to another.

Figure 18 shows the P-impedance attribute co-rendered with coherence attribute on the same stratal slices. Note how the lithology changes from mostly evaporites (high impedance) at the bottom of Nugget Sandstone to both sands and evaporites (Figure 18b) in the middle to mostly sands (low impedance) at the top of the formation. It is also evident in Figure 18b that the low impedance values are bounded by low coherence anomaly. This proves that the discontinuities that are seen in coherence attribute are actually the boundaries between the sand dunes and evaporite interdunes.

Self-Organizing Maps (SOMs)

Self-organizing maps (SOMs) are one of the best ways to classify seismic facies. SOM is one of the most used method of classification based on unsupervised machine learning, in geosciences (Zhao et al., 2016; Roy et al., 2013; Matos et al.; 2007; Saraswat and Sen, 2012). Seismic facies can be defined as 3D mappable seismic units composed of groups of reflections whose parameters differ from those of adjacent facies units (AAPG, 2019). Seismic facies are different from each other in terms of reflection parameters like configuration, continuity, amplitude, frequency, generally within the same depositional sequence. As such, there can be multiple sand facies with different porosity, color, mineral composition among other lithological characteristics. Since the general lithology of the subsurface in Nugget Sandstone is sands and evaporites, seismic facies classification can

give a lot of information about the subtle changes of lithology within the same sands and a pattern can be identified by looking at the gradual change of facies from sands to evaporites or vice versa.

Number of facies classes can be decided by the user based on the accuracy and detail they desire. The self-organizing maps take various attributes as input and combine them to represent the data in fewer dimensions of information, i.e., facies. For the purpose of this study, GLCM attributes including entropy, energy and homogeneity were used as input along with P-impedance to generate 120 seismic facies map co-rendered with coherence (Verma et al., 2018). Figure 19 shows the SOMs at deep, middle and shallow stratal slices similar to the ones used in coherence, curvature and P-impedance. In this figure, the proximal colors represent similar facies meaning similar rock type. The yellow seismic facies correspond to low P-impedance values (sands) and blue color correspond to high P-impedance values (interdunal deposits). Note how the SOMs illuminate the gradual change of facies between dunal and interdunal mineralogy.

Ant Tracking

Ant Tracking is one of the most important and efficient works done for the reservoir description and can help a lot in fracture or fault interpretation. There are two major advantages to using Ant Tracking technology. Firstly, it can swiftly describe the character of the fault development and plane distribution in the target area. Secondly, it can track discontinuity information in seismic volume, demarcate even the tiniest fracture and

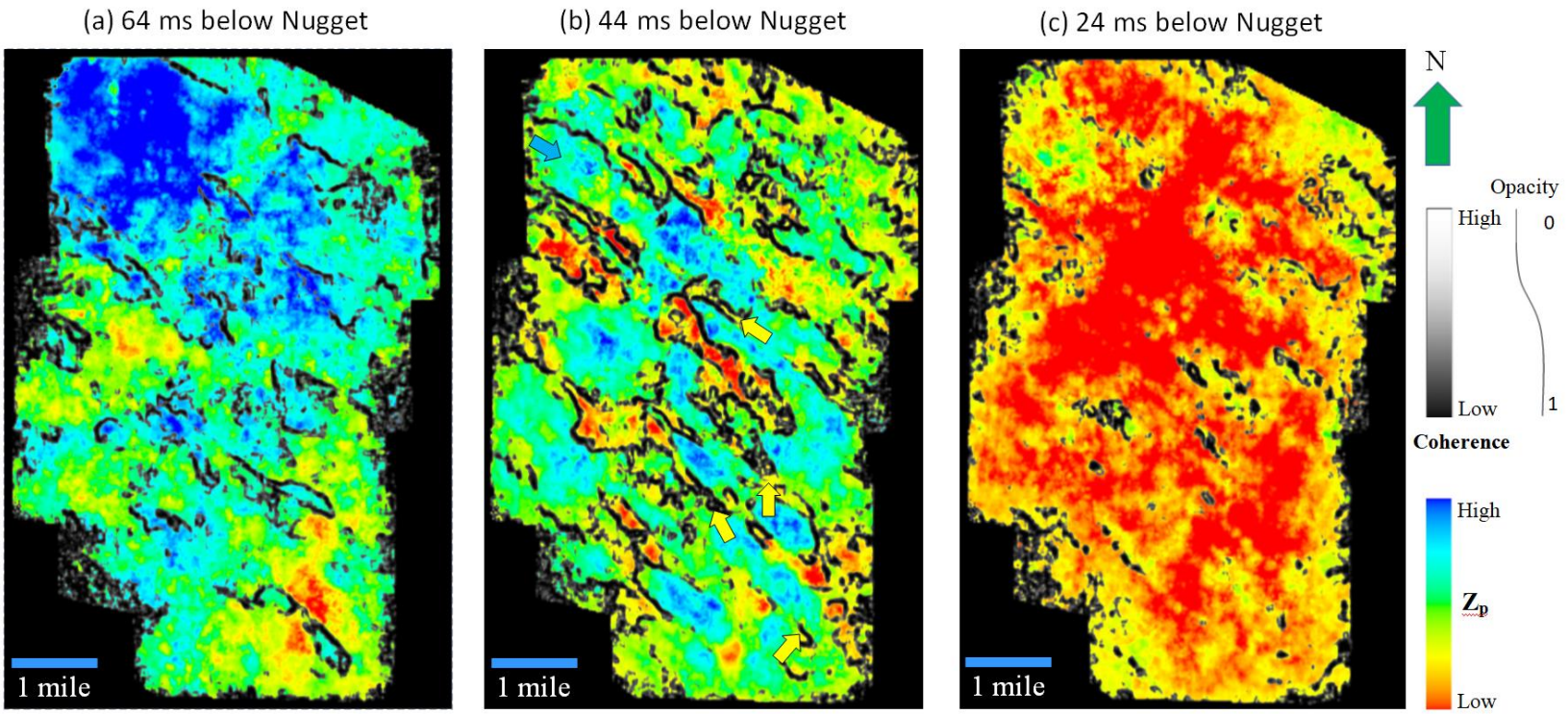

Figure 18: Stratal slices of P-Impedance (Z_p) co-rendered with coherence attribute. All slices are taken with respect to the Nugget Sandstone reflector. The eolian dune lineaments begin to appear 24 ms below Nugget (c), become prominent around 44 ms (b), and then start disappearing about 64 ms below Nugget (a). Note the blue arrow indicates the inter-dunal whereas the yellow arrow indicates the well-developed sand dunes. The co-rendered figure of curvature and coherence implies that the distinct features seen in coherence slices are surrounded by antiforms and synforms.

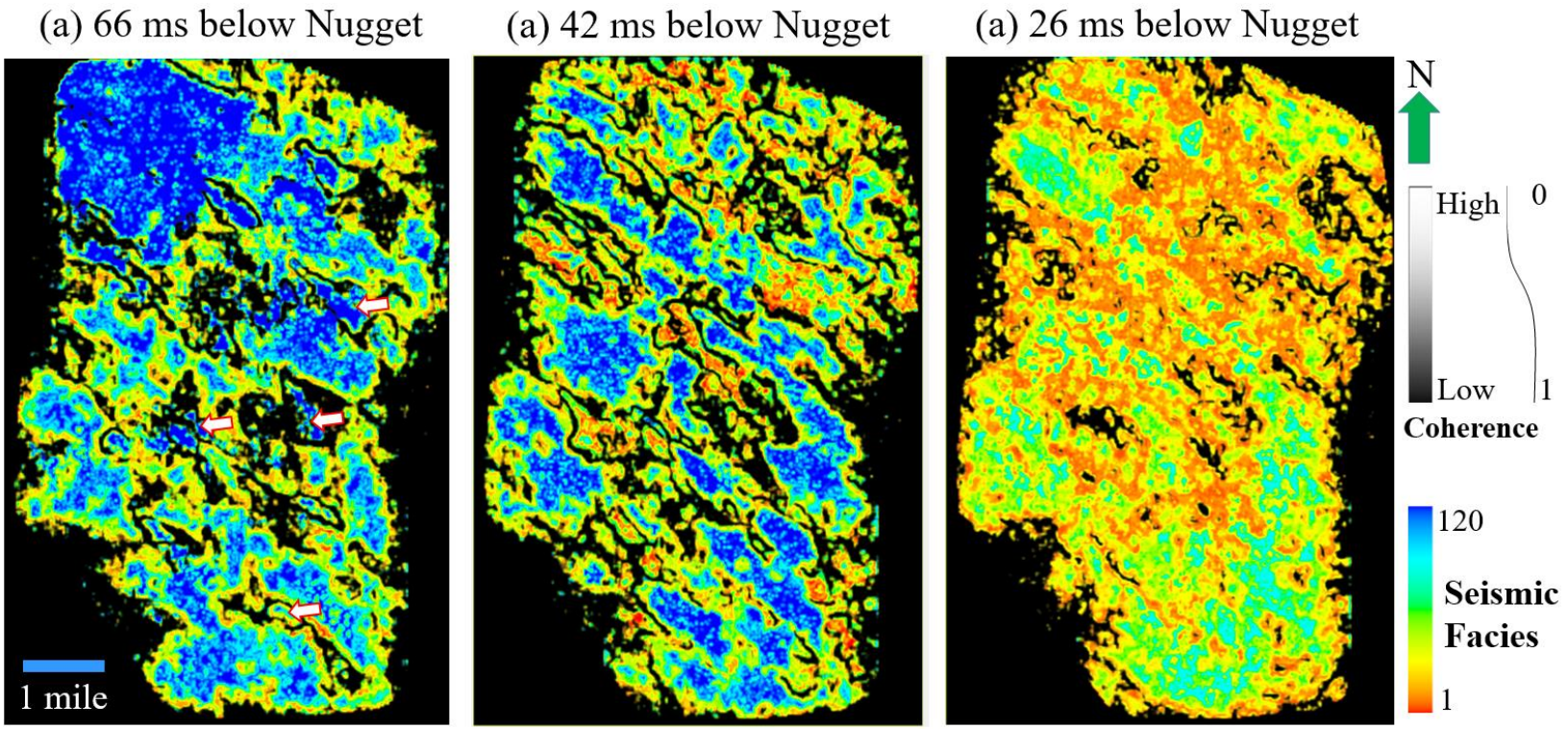

Figure 19: Stratal slices of the seismic facies, generated with self-organizing map algorithm (SOMs). All slices are with respect to the Nugget Sandstone top, the eolian dunes lineaments start appearing 66 ms below Nugget (a), become prominent (b) and then start disappearing around 26 ms below Nugget (c). Based on the correlation of P-impedance with seismic facies, blue colored facies represent interdunal deposits (evaporites) while yellow colored facies represent dunal deposits (sands).

determine the contact relationship of the space between the fractures (Xingxing et al., 2015; Silva et al., 2005).

As the name suggests, this algorithm is based on heuristic (automated learning) process by bionic (electronically biological) creatures, ants in this case, to achieve foraging behavior (search for food) in nature. This is an algorithm to implement fracture interpretation in 3D seismic data. The algorithm is very interesting and sows a lot of electronic "ants" in the data. These "ants" move along the fault plane and leave the "pheromone" behind. Other ants, being attracted by this "pheromone", concentrate around the fault plane to track it until the fracture tracking is completed.

There are 6 main parameters that can be modified using this algorithm. Each of the parameter is expressed in terms of the number of steps these "ants" can take and therefore is a natural number. The parameters are initial ant boundary, ant track deviation, ant step size, illegal ant steps allowed, legal steps required and stop criteria (%). Xingxing (2015) explains all these parameters in detail. For the purpose of this study, the Ant Track workflow was carried out in an interpretation software.

Figure 20 shows the Ant Tracking workflow applied to track the discontinuity surfaces and represent them as lineaments. The curvature attribute was used as the basis of this process and the lineaments represent the changes in the most positive curvature k_1 from positive to negative (Verma et al., 2018).

Since the paleo-wind direction is supposed to be perpendicular to these lineaments to form the sand dunes along these lineations, the strikes of all the lineaments were

calculated and added up to represent the paleocurrent direction on a rose diagram. The rose diagram is a circular histogram plot used commonly to display directional data and the frequency associated with each degree. The average wind direction comes out to be N-225˚ E which matches with the outcrop study done in the past (Figure 1) by Parrish and Peterson, 1988; and Chan and Archer, 2000.

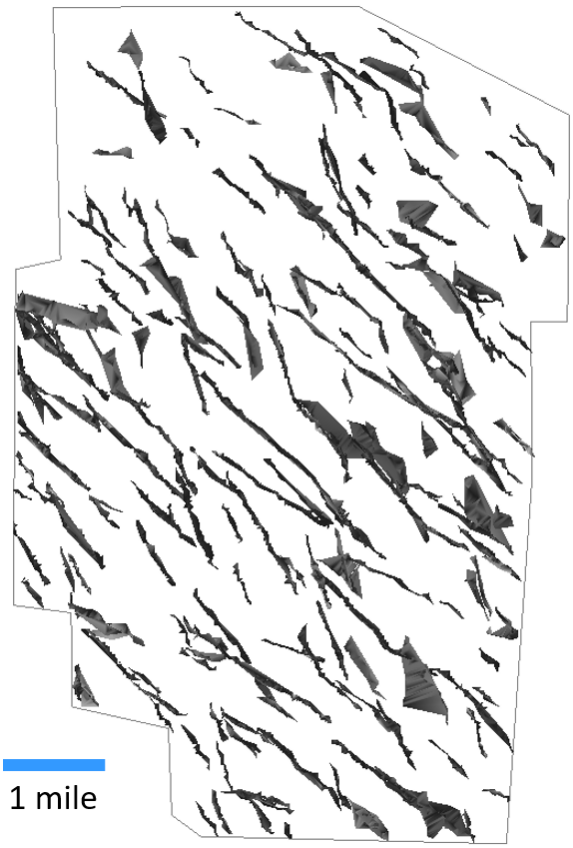

Figure 20: (Top) The discontinuity surfaces obtained by applying Ant Track workflow (Silva et al., 2005) on curvature k_1 volume (Figure). Note that all the small north to east striking lineaments were filtered out (Verma et al., 2018).

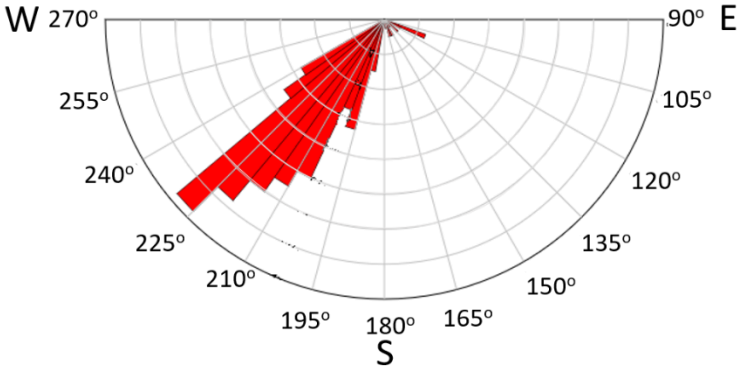

Figure 21: (Bottom) The rose diagram, showing the derived direction; which is simply the strike direction of the lineaments (Verma et al., 2018).

Chapter 6

SEISMIC DATA CONDITIONING

The previous chapter discusses all the seismic attributes that were used for this study. As the time progresses, so does the need to resolve thinner and thinner beds and map smaller and smaller reservoir changes. The modern world has started to extract as much information from the seismic data as possible and cost effectively at that. Hence the need and importance of all the attributes. However, it is important to realize that underlying these attributes, either prestack or poststack, are the gathers. The gathers are the basic building blocks of the seismic data and that is where majority of the information resides (Cook et al., 2016).

Seismic data conditioning can be defined as something that is often exercised to improve any quantitative seismic interpretation or reservoir characterization project. It is generally done to the pre-stack data but some of the processes can also be applied to the post stack data. These include various noise suppression techniques and other processes to get the data into a state that is suitable for inversion. Sometimes, gathers are calculated after each step of conditioning and attributes can be generated frequently to continuously monitor the effects of conditioning. This makes quality controlling (QC-ing) the seismic data easy and accurate.

Needless to say, conditioning of the gathers combines processing and interpretation to accurately characterize the reservoir and produce the best resolution data (that can be obtained) which matches the true reflectivity in both offset and time. Noise (unwanted

signal) is removed and artifacts from both acquisition and processing are removed to provide the most interpretable data possible. This brings forth the discussion between signal processing and signal conditioning. It is very important and yet hard to understand the exact difference between the two. The thing is there is sort of an overlap between the two.

Let us try to understand the difference through an example from an American's everyday life. Everyone knows how to make a coffee. One heats water, adds coffee powder to it, then adds milk to it (unless they like it black) and finally adds the sugar (unless they are trying to lose weight). These four steps are basically the same no matter where the coffee is made. This is called processing where each step is mandatory to get the final product. Sure, the order of these steps can be slightly changed like adding sugar before milk, but they still have to be done. Similarly, the signal processing is the process of converting input signal or data to output or desired product which is necessary for reservoir characterization or for any interpreter to understand.

Let us make a coffee once more. But this time, it will be the most perfect coffee made in the world. The quantity of the water used is exactly $3/4^{th}$ of the cup. It is heated for exactly 3 minutes 45 seconds at mid heat level on a stove. Exactly 2.5 sachets of the premium milk powder is added along with 2 tablespoons of the most expensive brown sugar. And voilà, you have the best coffee you have ever tried. This is called conditioning. Each step of this conditioning can be altered according to the user's taste and what he or she desires. Similarly, the signal conditioning refers to the process of making quantitative or qualitative changes to the signal to make it suitable and better for the next step of

processing. Therefore, signal processing is an implied step while the signal conditioning varies depending on the user's requirement or desire.

The main seismic processing steps from acquiring the raw field data to it being suitable for interpretation are – data input, reformatting, geometry assigning and binning, pre-processing, velocity analysis and NMO (normal moveout) correction, residual statics, preconditioning, stacking and migration. Since the seismic processing is not the focus of this study, all the steps will not be discussed in detail. However, the few seismic processing steps that were executed while performing the seismic data conditioning will be explained in minor details.

As mentioned earlier, the seismic data conditioning can be carried out on pre-stack or post-stack data. The pre-stack data conditioning can include – dense velocity picking (residual NMO correction), denoising, demultiplying, Q (seismic quality factor or anelastic attenuation factor) compensation, residual trim statics correction, wavelet destretching, post-stack matching, zero phasing, angle stack generation, structurally oriented filtering (SOF) and so on. The post-stack data conditioning can include – stack alignment, structure-oriented filtering (SOF), structurally conformable filter (SCFIL) among others (AASPI 2019).

The pre-stack time migrated gathers were shared by University of Wyoming along with the migration velocity data file. The migration process is performed to take care of the dipping reflectors. Because of the geometry of the sources and receivers (geophones) involved in the seismic acquisition survey, the dipping reflectors appear to be flatter and

shallower than the real subsurface geology. After migration is performed, the reflectors become steeper and deeper than before and are shown in correct positions. The steps performed in this study are NMO (normal moveout) correction, stacking, calculation of volumetric dips, filter dip components, similarity attributes, pre-stack structure-oriented filtering (SOF), restacking, recalculation of volumetric dip, filter dip components and similarity attributes. Each of these steps are discussed below.

NMO Correction

NMO stands for normal moveout. As the offset (distance between the source and receiver) increases, so does the time taken by a seismic P-wave to travel. In seismic acquisition, each subsurface point is mapped multiple times with different source-receiver geometry. The point being mapped is referred to as common midpoint (CMP) as can be seen in Figure 22 below. The number of times a single subsurface point is mapped is called the fold of the seismic data. For example, the number of folds in Figure 22 is 6. Now-a-days the seismic surveys have folds as high as 1000, sometimes even more.

The folds are calculated by following formula:

*Number of folds (f) = (1/2) * (No. of geophones*Source separation) / (Receiver separation)*

The common source separation is 120 ft. Because of the increasing time taken by the wave to travel, the relationship between the arrival time and offset is hyperbolic (Figure 23). The normal moveout takes care of this issue by virtually bringing the mapped subsurface point directly below the source such that the offset becomes 0 (source and receiver at same point).

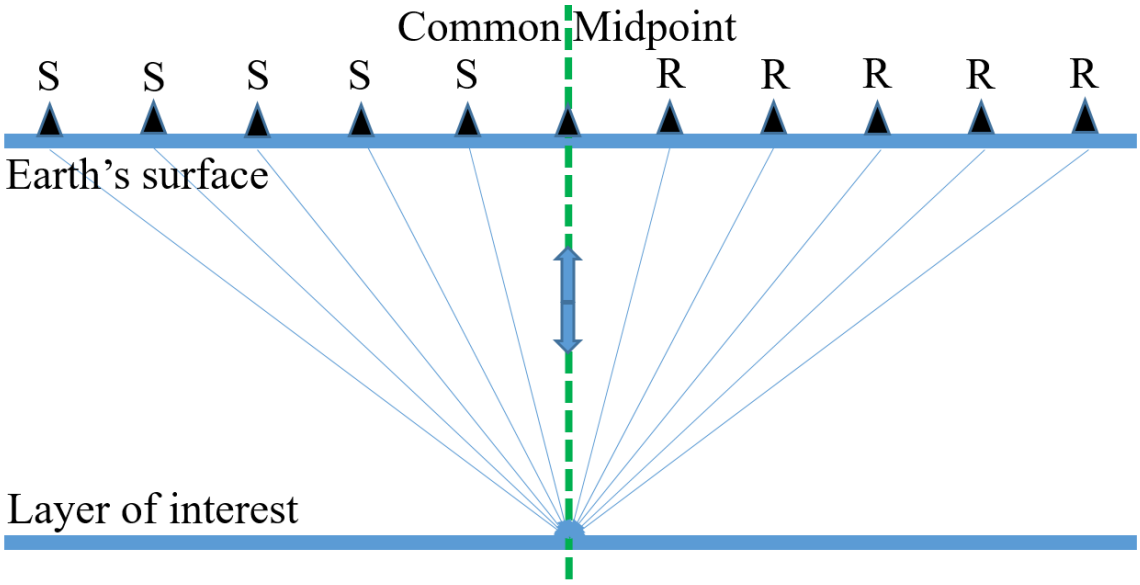

Figure 22: Seismic acquisition with 6 folds, S stands for source and R for receiver

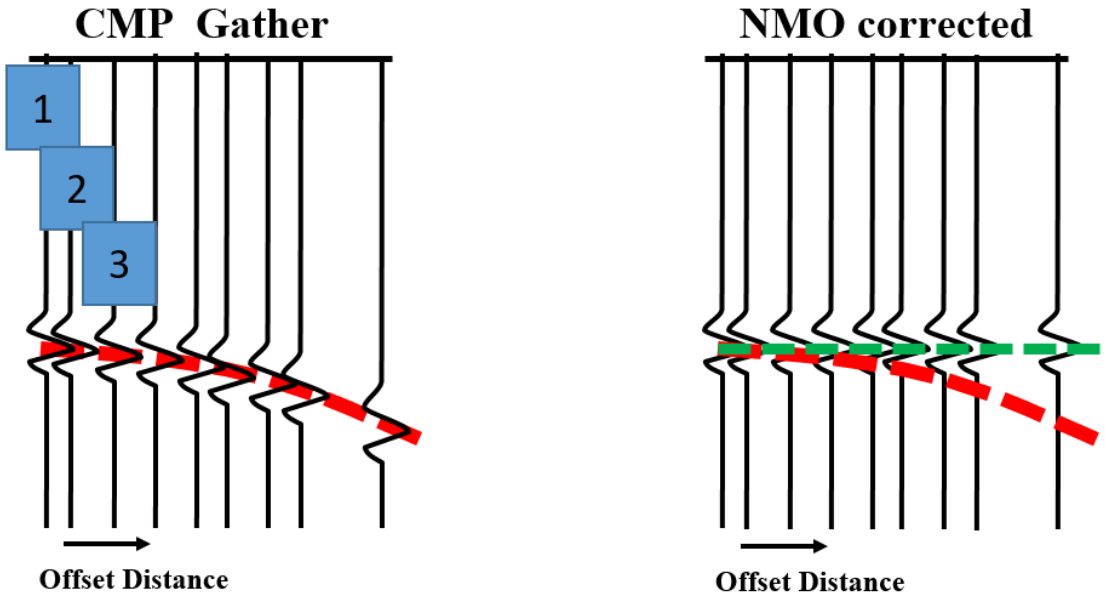

Figure 23: Pre-stack data before (red) and after (green) NMO correction (course slides)

For a flat, horizontal reflector, the travel time equations is:

$$t^2 = t_0^2 + (x^2/v^2) \quad , \tag{3}$$

, where t = two-way travel time for a particular offset, x = offset, v = velocity of medium above the reflector, t_0 = two way travel time at zero offset.

To perform NMO correction, velocity model of the survey is generated by looking at the semblance plot. The semblance plot is a hyperbolic Radon transform, in which amplitudes are smoothed, scaled and contoured to produce a virtual display. This transformed display has axis of time and velocity that are used to identify the velocities for NMO correction of the CMP gathers (Cao and Bancroft, 2004). The velocity picking is not explained in detail here as the velocity model data was already provided for this study.

Stacking

The stacking process is fairly easy to understand. After the NMO correction is carried out, the only difference between the traces is the different offset. They are really redundant samples of the same reflection. These traces are then added up and normalized to generate a single trace. This increases the signal to noise ratio because the incoherent (random) noise is present at different times in different traces but the signal (which is the one single mapped point) is present at exact same time-depth. So basically, the stacking process generates a stacked section – one trace representing each midpoint location assumed to have been recorded with a shot and receiver coincident at the midpoint location (AAPG, 2019; Figure 24).

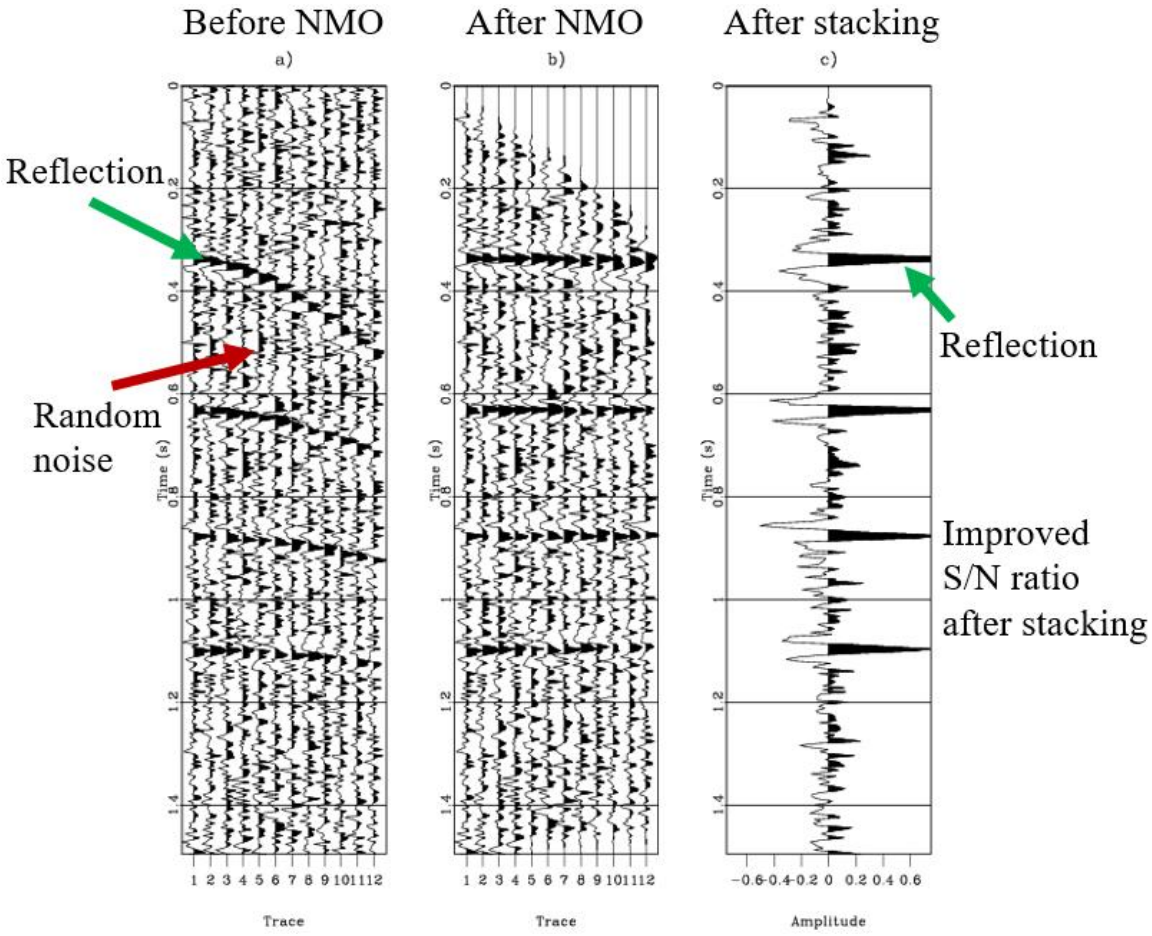

Figure 24: All traces of a single common midpoint stacked together to a single trace with reduced incoherent noise and improved signal to noise (S/N) ratio (UTPB course slides)

Volumetric Dip

Volumetric dip calculations are needed for almost every seismic attribute calculation. The calculations include inline dip, crossline dip, dip magnitude, dip azimuth, and a confidence measure of these estimates. The inline and crossline dips are the critical components to calculation of coherence and curvature seismic attributes which have been discussed earlier. All the measurements are done directly from the post-stack seismic

amplitude volume. The confidence volume is used in the next step of filtering dip components to remove artifacts in the dip volumes. The dip is the first derivative of the surface. And the curvature attribute discussed earlier is the second derivative of surface and first derivative of this dip.

Filter Dip Components

The inline dip, crossline dip and confidence are used as input for filtering the dip components. The results are filtered components of inline dip, crossline dip, dip magnitude, dip azimuth and a new confidence estimation. The computed confidence in this process or previous basic dip calculations is simply the semblance along dip of the analytic traces (AASPI, 2019). This process can be iterated multiple times with the output of first iteration being used as the input for the second iteration and so on until the desired filter output is reached. Note that performing this more than a few times without continuously checking the results may result in loss of signal as the dips are smoothed and filtered over and over. Two to three iterations is a suitable number to execute.

Similarity attributes have been discussed earlier in the form of sobel filter or coherence. The input to calculating similarity are inline and crossline components (filtered if possible) of reflector dip and the seismic amplitude volume (stacked). Similarity attribute is needed as input for performing the pre-stack structure-oriented filtering (SOF) which is discussed next.

Structure-Oriented Filtering (SOF)

The general name for SOF process is edge-preserving structure-oriented filtering (Luo et al., 2002). It can be performed on pre-stack or post-stack data or both. However, the effects of applying this on pre-stack data are more pronounced than applying just on post-stack because of the stacking process that is carried out after this is applied. Performing SOF on pre-stack dataset, affects each trace of a common midpoint (CMP) which in turn affects the stacked trace more than applying it on a single stacked trace in post-stack data.

The structure-oriented filtering (SOF), when applied on the pre-stack data during seismic processing, improves the overall data quality and increases the resolution of the discontinuities seen in the coherence-based attributes. After SOF, the time slices look sharper with preserved discontinuities and suppressed acquisition footprints.

The objective of this process is to remove noise by applying a dip-field based, structurally aware filter. The structure-oriented filtering (SOF) process smooths along structural planes as defined by a dip field. It is essentially dip-aware smoothing. It is an effective method of removing incoherent noise and improving continuity of events, without smoothing across dipping planes (Fehmers et al., 2003). The parameters control the number of traces to be combined in the inline and crossline directions.

An important thing to note here is that the structure-oriented filter can be applied along structure, along structure and offset, along structure, offset, and azimuth, along offset and azimuth, or only along azimuth (AASPI, 2019). The rejected noise (filtered out data)

can also be obtained as the output of SOF if needed (Figure 25). Sometimes, the changes in the seismic data after SOF are so minor, that they are hard to notice with naked eye. By looking at the rejected noise, the geophysicist can determine whether the parameters they used for SOF are significant enough or not and modify them in next iteration.

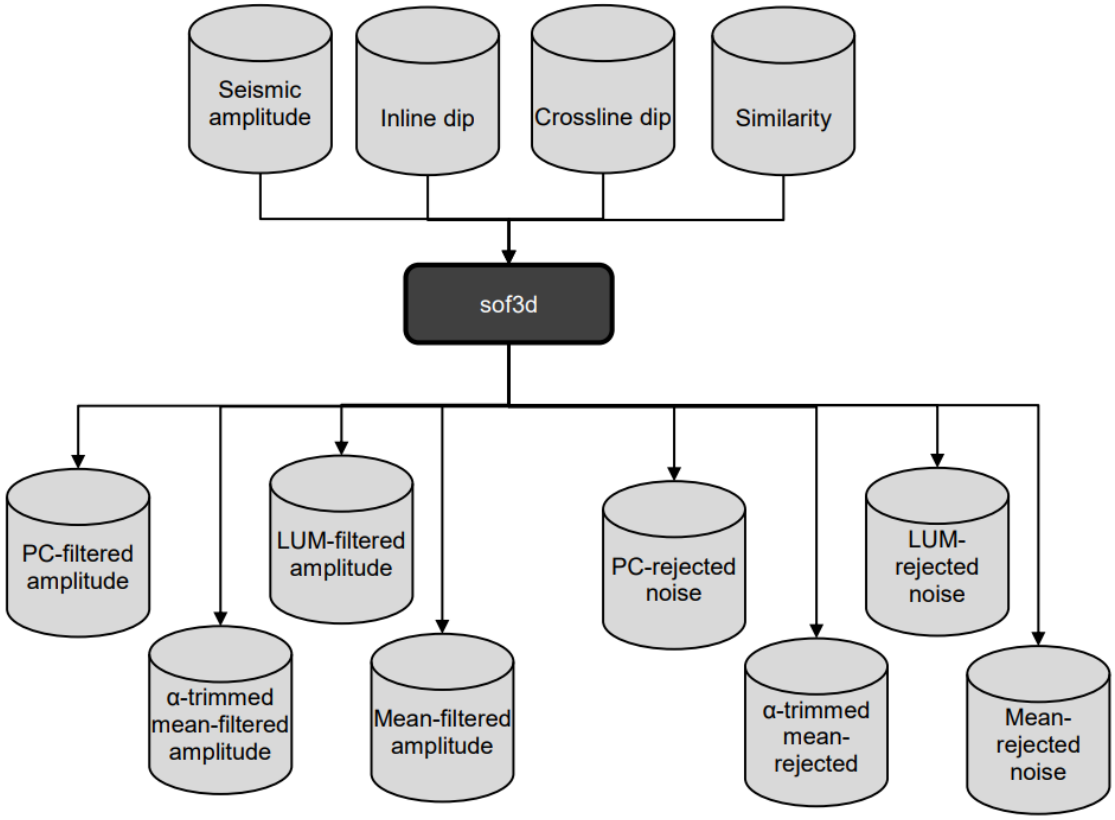

Figure 25: Flowchart exhibiting the inputs and outputs associated with the structure-oriented filtering (SOF) (AASPI, 2019)

Pre-stack SOF parameters

The primary parameters which are altered for deciding the best structure-oriented filter for the dataset are window height (s), inline and crossline window radius (ft), offset

window radius (number of traces), preferred similarity range (s_low and s_high along with s_centered_window). Another very important factor impacting the result is the type of filter used and it is decided based on the desired accuracy level. The higher the accuracy, the more sophisticated the filter required, and therefore the more the amount of time one needs to spend which in turn depends on the number of processors and processor speed. For example, LUM (lower-upper-median) filtered data takes less time and gives decent result but PC (principal-component) filtered data takes a lot more time and gives sharper results. For the purpose of this study, PC filter was used during SOF.

Oftentimes, it is a good idea while filtering manually or performing any seismic conditioning in general to test changing one parameter at a time while keeping others same. When the best result for that particular parameter change is obtained, the value of that parameter is kept the same while the second parameter is modified until the best result is achieved and so on. This method of testing each possibility sequentially in order to determine the best solution is called exhaustive search or direct search. Sometimes, this method is also referred to as the “brute force” method. It is called so because this method is generally used when applying the filter manually, while now-a-days with the advent of machine learning, there are other faster methods being developed.

It is important to note that the larger the window height (half-window distance), the more it will tend to emphasize large and strong events and tend to remove short and stubby reflections and noise. This is also explained in curvature attribute that a syncline for small wavelength can be a part of a bigger anticline (longer wavelength, Agrawal et al., 2018).

The inline and crossline window radius can be individually changed for SOF. It determines how many traces are included which is equal to the number of Kuwahara windows used. The Kuwahara filter is the basis of the SOF performed on this study (Kuwahara et al., 1976). Since the inline and crossline distance in this seismic survey is 120 ft, if this is kept as inline and crossline radius, only 1 inline and 1 crossline will be filtered at a time (smaller structural features will be the focus). Both the computation time and the strength of the filter increase with increasing window size. For good quality data, a more effective workflow is to iteratively smooth using smaller windows rather than double the window size in both directions. Such smaller windows not only follow curving reflectors better but also implicitly taper the filter towards the edges (AASPI 2019). The offset window radius determines the filtering in the offset direction and is 0 for post-stack SOF because the traces are already stacked. However, as mentioned earlier, applying SOF on pre-stack has advantages over post-stack. The filter can be applied in pre-stack in offset direction by changing 'offset window radius or size' to 1 trace(s) or more.

The similarity ranges can be changed to decide the extent of filtering. If the value of similarity attribute at the analysis point is below the threshold ($s<s_{low}$), no filtering takes place and the filtered data are assigned weights of $w=0$. Similarly, if the value of the similarity attribute at the analysis point is above the threshold ($s>s_{high}$), the filtered data are assigned weight of $w=1$ such that the filtered data replaces the original data on output. And if the similarity attribute at the analysis point falls between the two ($s_{low}<s<s_{high}$), the weights of the filtered data are $w=(s-s_{low})/(s_{high}-s_{low})$, and a linearly weighted average of the filtered and unfiltered data takes place. If $s>s_{centered}$, the filter applied is

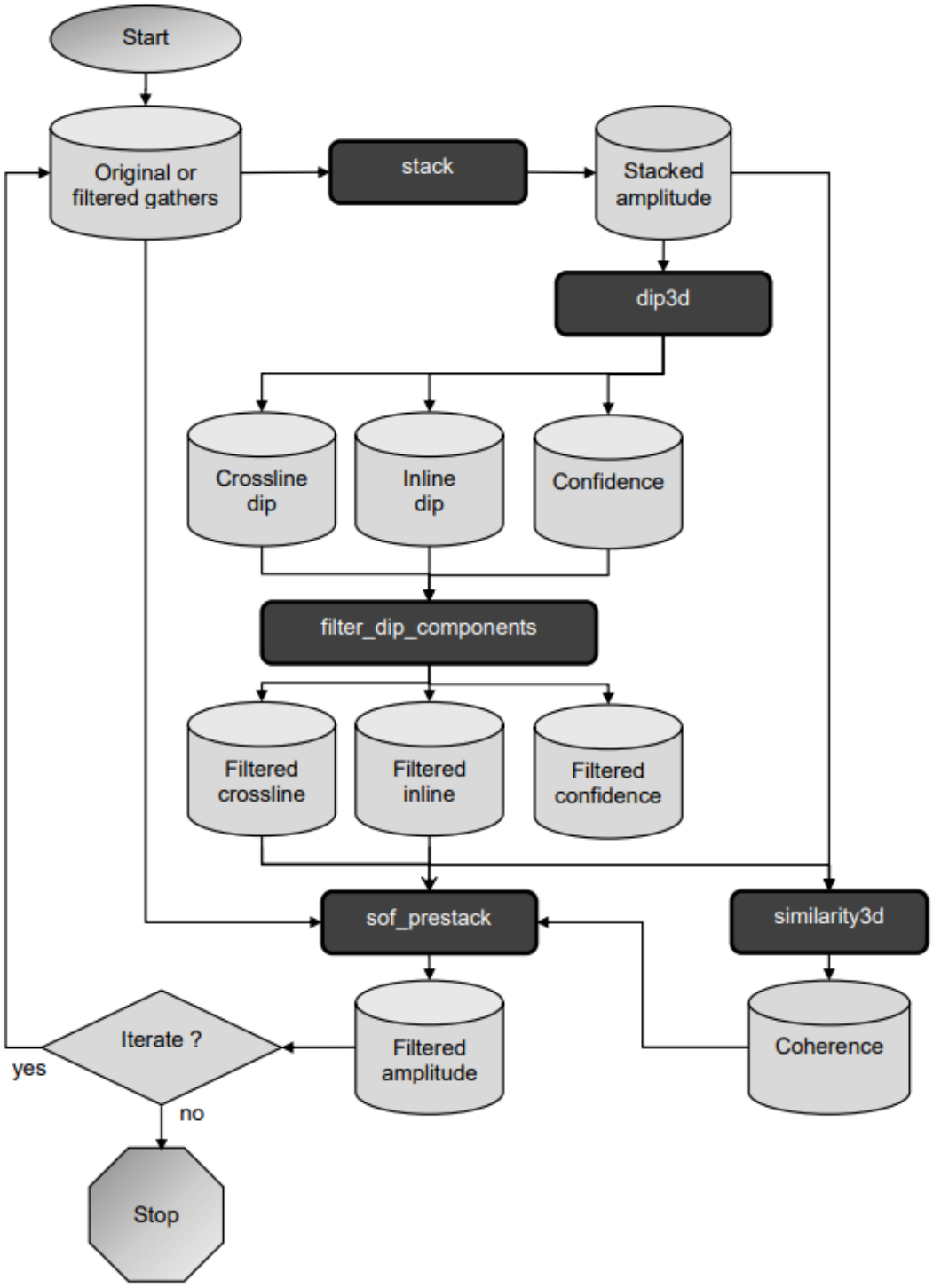

Figure 26: Flowchart exhibiting multiple iterations of structure-oriented filtering

(AASPI, 2019)

centered about the analysis point (AASPI, 2019). For this dataset, the variation in similarity ranges hardly affected the filtering process.

The output of the SOF can be used as the input to the 2nd iteration of SOF. But it is better to go through the hoops of stacking, calculating dips, filtered dips, similarity and then do the 2nd iteration because this way the dips are updated to represent the improved fidelity of the filtered data.

For the purpose of this study, both LUM-filtered and PC-filtered data were tried first (Figure 27). The inline and crossline distance for this survey is 120 ft. The inline and crossline window radii (ft) that were tried were – 120, 240, 360, 480, 600 and 720 (Figure 28). Window heights were tried from 0.01 to 0.1 second (Figure 29). The offset window radius was kept to 1 trace. The similarity ranges (s_low and s_high) tried were – 0.001-0.002, 0.002-0.003 and so on until 0.4-0.5. Three iterations of SOF were tried, taking output from previous iteration as input for the next (Figure 30). Also, during successive iterations, filtered dip components were used. All the parameters were modified and tried on a cropped dataset and the parameters that showed the best results were finally applied on whole dataset.

The final values of the parameters that gave the best result are:

Window height (s): 0.03

Inline window radius and crossline window radius (ft): 240

Offset window radius (no. of traces): 1

s_low: 0.2 s_high: 0.3 s_centered_window: 0.95

Type of filter: Principal Component (PC)

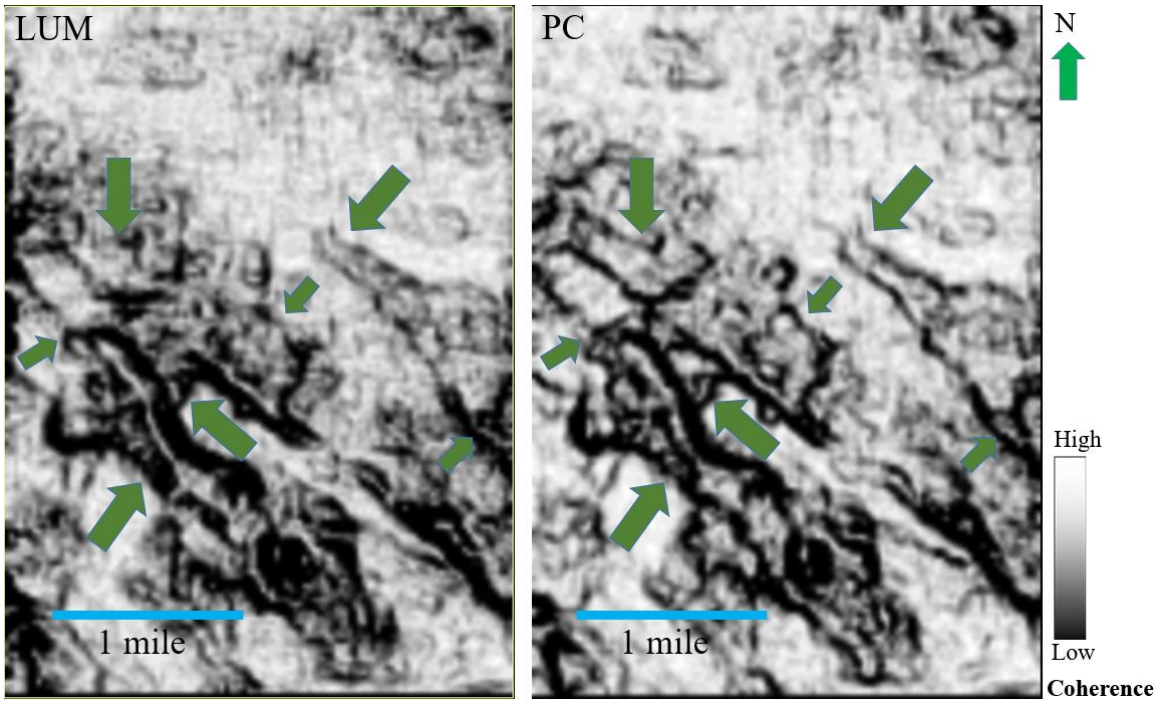

Figure 27: Comparison of coherence slices for LUM and PC filter applied to the cropped dataset. The green arrows show few features that are better illuminated in PC filter than LUM filter.

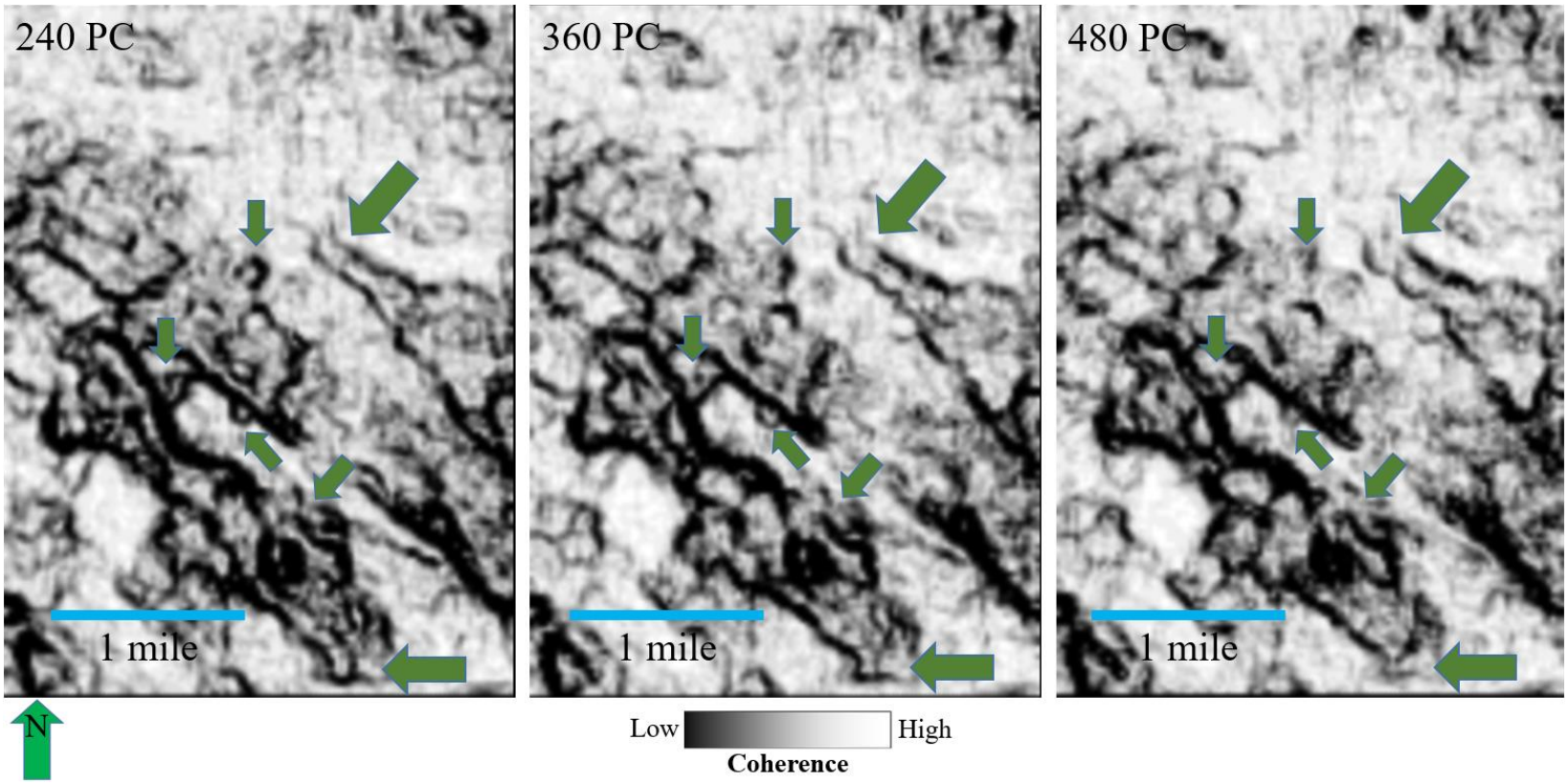

Figure 28: Comparison of coherence slices for various inline and crossline window radii for the cropped dataset. The green arrows show few features being very sharp and clear in 240 ft window, less sharp in 360 ft window and hardly visible in 480 ft window. PC filter was used for all.

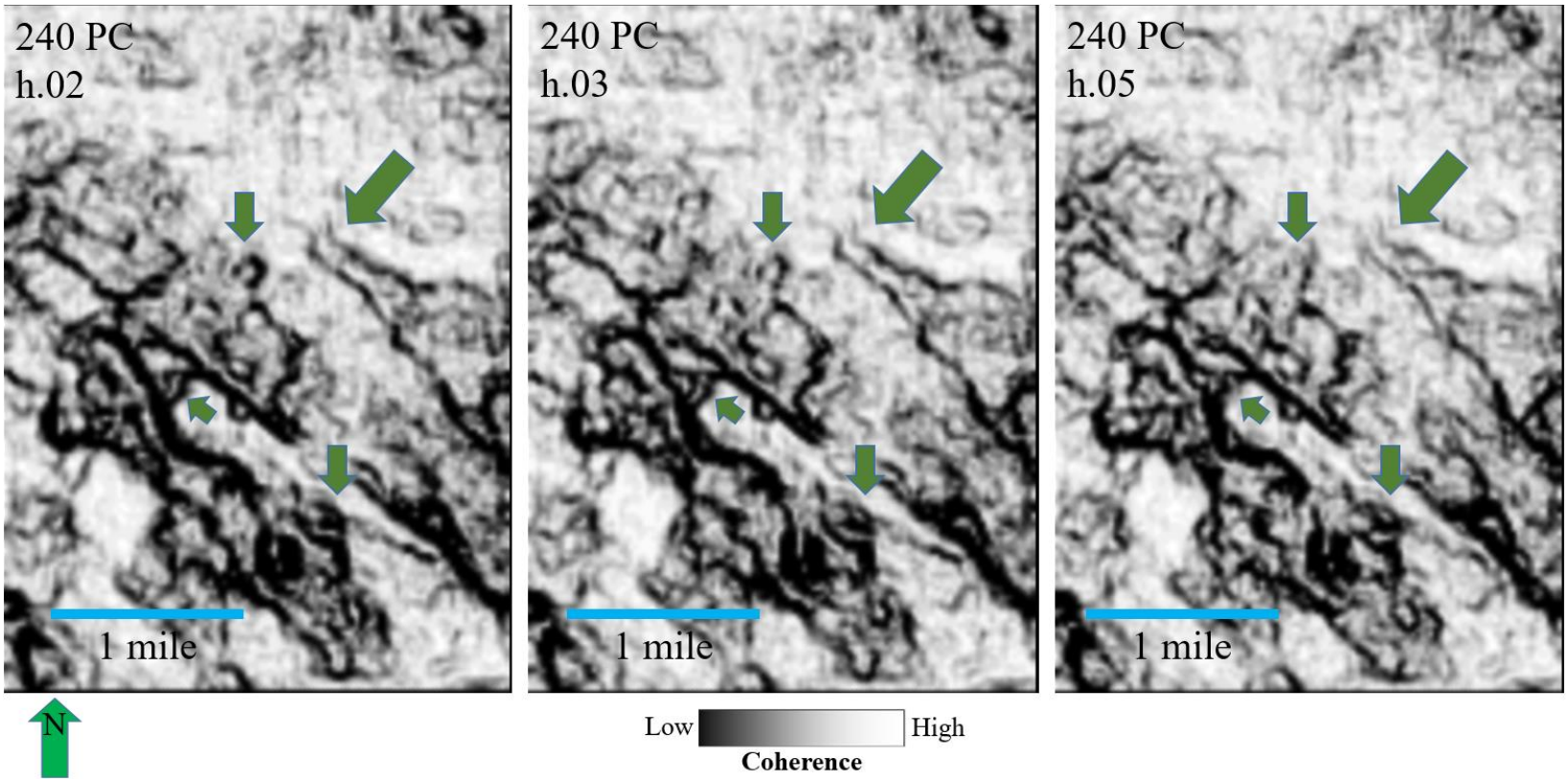

Figure 29: Comparison of coherence slices keeping previous parameters same and changing the window height (s) for the cropped dataset. Note how the structures become clear going from 0.02 s height to 0.03 but start disappearing as the window height is increased further to 0.05 s. As a result, 0.03 s window height was chosen as the best value.

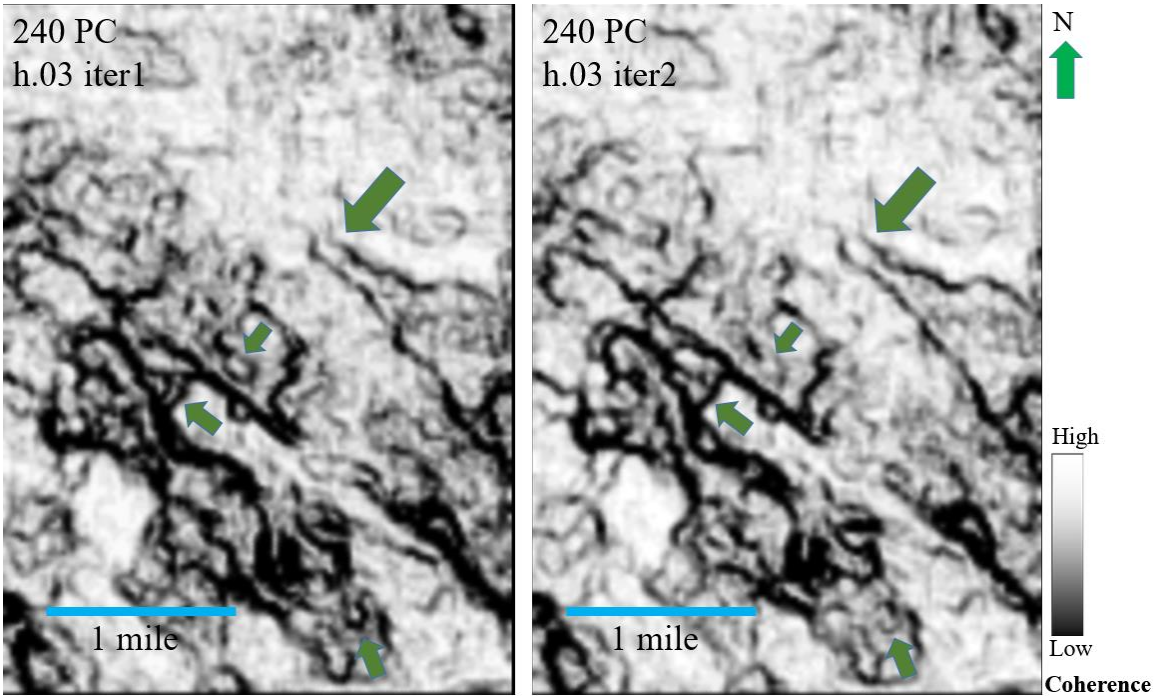

Figure 30: Comparison of multiple iterations of SOF in coherence slices keeping all previous parameters same. The 2nd iteration was applied using the output of 1st SOF as input for 2nd. Note how the structures become vague and start disappearing in the 2nd iteration. This is because of over-smoothening. As a result, iteration 1 was the best choice.

After the final parameters were chosen, SOF was applied on the whole dataset (Figure 31). There is some signal that goes missing during the seismic conditioning because of the smoothening that happens during the process. But those minor features are insignificant when trying to resolve and understand the bigger sand dunes.

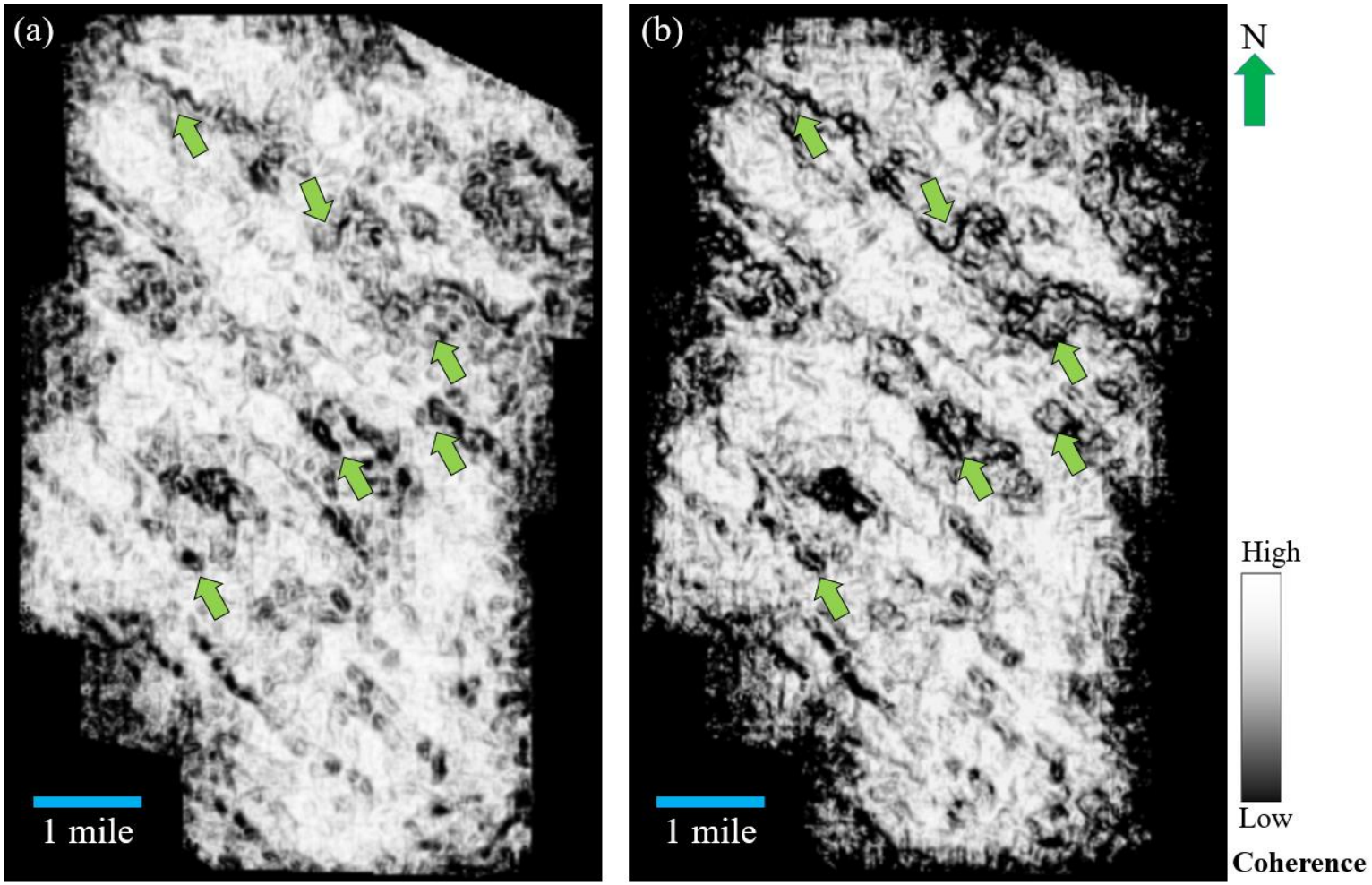

Figure 31: Stratal slices of the Coherence attribute before and after the seismic data conditioning (both are 24 ms below Nugget). The green arrows indicate the features which look sharper and more resolved after applying structure-oriented filter (SOF).

Chapter 7

DISCUSSIONS AND CONCLUSIONS

The Nugget Sandstone is an eolian deposit, characterized by dunal and interdunal deposits. The formation was deposited as part of the Early Jurassic sand sea that covered Arizona, Utah and southwestern Wyoming. While Wyoming and Utah seem to have more sand formations, sand dunes are surprisingly rare in Arizona. The Nugget Sandstone is known by the name of Navajo Formation in Utah and Arizona.

A high correlation in the well to seismic tie with the well A of about 65%, confirms that the lineaments seen in the seismic data are within the Nugget Sandstone. While the thickness of the Nugget Sandstone (~500 ft) remains the same in the seismic survey area, the formation top dips down from about 12,500 ft to about 13,500 ft going north to the south of the survey. The petrophysical analysis indicated that the Nugget Sandstone interval consists of sandstone (dune deposits) and clay along with carbonates (interdune deposits).

Multi-well analysis (well A and well B) suggests that the overall lithology of the Nugget Sandstone may be uniform (i.e. sandstone); however, there is a significant amount of internal heterogeneity present in the wells that can be correlated laterally. While well C shows more quartz rich sands and less evaporites, well A, on the contrary, shows more evaporites and less sands. The presence of evaporites is fairly common in the sand dunes area. They originate from the dried off ephemeral lakes that are responsible in making the sand dunes stable along with rain water. Because of this, the interdunal areas with more

evaporites are often associated with high bioturbation. Another possible reason is the depth of water table in the interdunes compared to the dunes.

Coherence and curvature (seismic) attributes show NW-SE lineaments in Nugget Sandstone. The seismic attributes also indicate that the structures or funny looking things (referred to as FLTs at the beginning of the study) start appearing about 65 ms below the Nugget top, become prominent in the middle of the Nugget Sandstone and start disappearing towards the top (about 20 ms below Nugget). Acoustic impedance and petrophysical analysis helped in discriminating dunal and interdunal deposits with evaporites at a lower elevation (interdunal) than the sands (dunal).

The seismic facies calculated based on the self-organizing maps (SOMs) also prove the presence of more sand facies at the top of Nugget Formation and more evaporites and carbonates at the bottom. The bump map clearly delineates the sand dunes within the discontinuous features we saw in coherence. Comparing the shapes of sand dunes seen from the bump map to other types, it is quite evident that these lineaments correspond to the transverse dunes, and the predominant paleo-wind direction resulting in formation of these dunes would be NE-SW.

The ant tracking workflow, based on the most positive curvature (k_1) in the zone of interest, tracks all the discontinuity surfaces and shows them as the lineaments. The wind directions, perpendicular to these lineaments, are added up to show an average direction of around N-225˚ E which supports the previous outcrop studies. Based on the lithology, porosity, fluid saturation, and vertical and lateral extent of the Nugget Sandstone, it appears

to have a good potential for carbon storage. The sequestration site is perfect for the nearby located Naughton Power Plant (Figure 3) and can be tested right away.

Modern-day Analog

There are various sand dunes around the world different in size as well as types. Some examples of the world's record-breaking sand dunes are: Great Dune of Pyla (La Teste-de-Buch, France), Dune 7 (Namib Desert, Namibia), Star Dune (Great Sand Dunes National Park & Preserve, Colorado), and Simpson Desert Dunes (Australia). But for the purpose of this study, there is no better modern-day analog than Rub al-Khali.

The Rub al Khali is the largest uninterrupted expanse of sand desert in the world, and the driest. Part of the Arabian Desert, the Rub al Khali, means 'empty quarter' in Arabic. It lies in a structural basin and extends across an area of about 250,000 mi^2 (Abuwala, 2017). It is located mainly in Saudi Arabia with parts in UAE, Yemen, and Oman. The elevation above sea level is about 2,000 ft in the west and comes down to 600 ft in the east. The grain size also goes from sands in the west to gravel and gypsum in the east.

What makes this a great analog to the Nugget Sandstone is the presence of calcium carbonate, gypsum, and clay that were shallow lakes 6,000 to 2,000 years ago. The flora and fauna fossils can also be found at the site of dried-up lakes. Rub al-Khali has tremendous reserves of oil and natural gas. One of the largest oil field in the world, Al-Ghawar, and another significant reservoir called Al-Shayba are both located in the Rub al Khali.

Figure 32 shows a current (Google Maps, 2019) satellite image of this ‘empty quarter’. The first thing to notice here is that these are transverse dunes which are similar to this study. The wind direction (shown by blue arrow) is east to west which is evident by the gradual dip (stoss side) on the right and steep dip (lee side) on the left of each sand dune. Secondly, the scale of the sand dunes is also similar. It is hard for commoners to imagine that the sand dunes can be as high as 100s of ft and they can be as distant as 2 miles from each other. But the scale in Figure 32 shows how huge these are.

Another thing to notice here is the interdunal area. Even in the satellite image, the interdunal areas look like they have water filled in them separating each sand dune when actually this picture is taken in the currently dry region. As mentioned earlier, most sand dunes are stabilized by the presence of water which gets seeped into the interdunal areas and eventually dries off. The evaporites left behind are responsible for this surprising reflection giving it an appearance that Rub al-Khali was filled with water at the time this picture was taken. So, just like the study area, this picture shows transverse dunes with almost same scale and with interdunal areas being evaporites.

The yellow stars A and C represent the relative positions of wells A (Keller 1-12) and C (AGI 2-18). Note how it is possible for well A and C to be in different parts of the environment. A will have more sands and is in dunal area while C has more evaporites and is situated in interdunal area which explains the internal heterogeneity evident from the petrophysical analysis of the study.

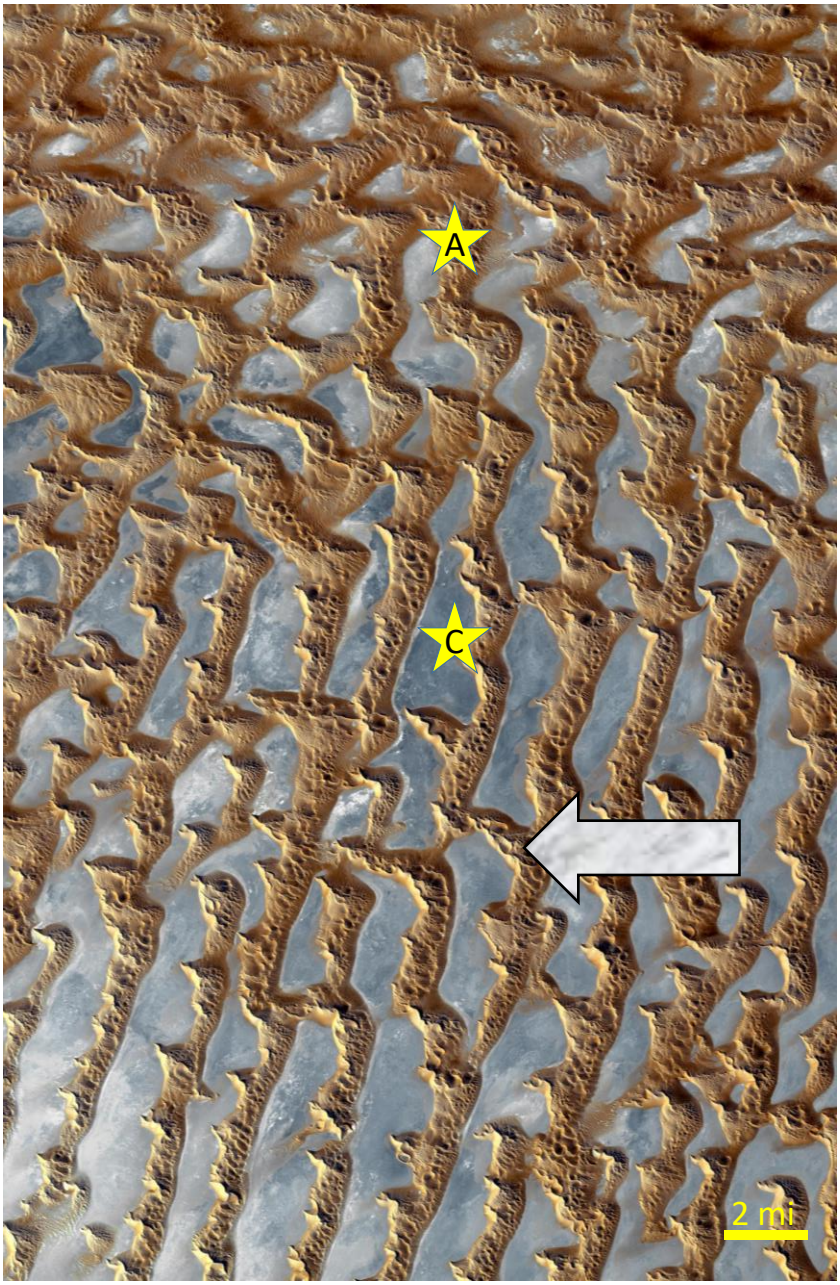

Figure 32: Satellite image of Rub' al Khali, Arabia – one of the largest desert in the world. The white arrow shows wind direction, brown color shows dunes and blue/white color shows interdunes (modified after ASTER, 2005). The stars represent the approximate analogical relative location of wells A and C in a dunal/interdunal deposit area.

Future Work

Even though a lot of light has been shed on the Nugget Sandstone and the available seismic survey during this study, due to time constraints, not everything that was thought or discussed could be executed. This section also includes the invaluable feedback that was given by academic as well as industry experts during the times this study was presented as a poster or an oral presentation over the duration of 2 years in various conventions, symposiums and conferences.

The first thing that can be performed in the future is computing spectral decomposition. Every seismic survey can be decomposed into multiple spectral components. Each spectral component illuminates a different aspect of the survey and may be beneficial in extracting more information about reservoir lithofacies and fluids. For example, near offset seismic stack is similar to zero offset section and gives an estimate of normal incidence acoustic impedance. The far offset, on the other hand, can determine the relationship between V_P and V_S which determines the elastic impedance attribute of the rock layer. The spectral decomposition can be performed on the basis of frequency, phase, offset range, angle stacks and so on. This definitely is the next step to go through on this seismic survey.

The second thing to think about is the type of hydrocarbon or the reservoir quality of the Nugget Sandstone. It is deduced that the Nugget Sandstone is a far better formation for carbon sequestration than it is for hydrocarbon exploration. Even so, it is yet to be determined, how big or small the potential of the sequestration is present here. If it can be

determined from seismic and well data that the potential is huge, than this will be a huge discovery and a relief to Naughton Power Plant which can start storing its produced CO_2 in this nearby formation.

The third thing to think through is what would be a better way to charge the reservoir. Is horizontal drilling better than vertical drilling? It seems quite logical that since interdunal areas are filled with evaporites with high impedance and low impermeability, the wells should be drilled into or along the sand dunes instead. But it is not very clear, exactly how much the porosity and permeability of sands in this formation is different from that of evaporites since it is a heterogeneous formation overall. Also, it is necessary to determine the exact length of sand dunes to determine the volume of the reservoir considering the depth of formation is changing too.

The last thing I can personally think of, that can be studied here is the effect of the winds. It was great to determine the wind direction by looking at the seismic attributes. Since winds are responsible for the formation of sand dunes, they might be affecting the porosity of the sands in a particular direction. This leads to a discussion of anisotropic or linear change in the porosity and permeability of the dunes and the Nugget Sandstone in general. If this is figured out, it will give a much easier time to the well planners. Again, since winds are the primary factor in formation of sand dunes, the height of sand dunes or the quantity of sands can actually be used to determine the strength or magnitude of the Early Jurassic wind in this area.

And then there are certain unanswered questions which can be debated over a healthy discussion. Do the prevailing winds of Early Jurassic matches with modern world (it should because wind currents are eventually the result of earth's motion from west to east)? What kind of water source led to deposition of evaporites in the Nugget Sandstone other than simply the rainfall? What exactly happened after the dunes were deposited and stabilized with water, how are they still preserved in the seismic survey? Are evaporites generally present at this ridiculous depth of 13,000 ft all over the world?

While these future computations, suggestions and questions seem overwhelming now, I hope someone will figure them out after me.

REFERENCES

AAPG, 2019, https://wiki.aapg.org/Main_Page; accessed April 2019.

AASPI, 2019, http://mcee.ou.edu/aaspi/documentation.html; accessed April 2019.

Abuwala, A., 2017, https://www.worldatlas.com/articles/rub-al-khali-empty-quarter-of-the-arabian-desert.html; accessed April 13, 2019.

Agrawal, D., B. Lujan, S. Verma, and S. Mallick, 2018, Peculiar geological features in the Nugget Sandstone of the Moxa Arch: 88th Annual International Meeting, SEG Technical Program Expanded Abstracts 2018, pp. 1813-1817.

Archie, G. E., (1942), The electrical resistivity log as an aid in determining some reservoir characteristics, Petroleum Transactions of AIME. 146: 54–62. doi:10.2118/942054-g.

ASTER, 2005, NASA's satellite image of Rub' al Khali, Arabia, https://www.nasa.gov/multimedia/imagegallery/image_feature_1200.html; accessed December 10, 2017.

Augustyn, A., P. Bauer, B. Duignan, A. Eldridge, E. Gregersen, J.E. Luebering, A. McKenna, M. Petruzzello, J.P. Rafferty, M. Ray, K. Rogers, A. Tikkanen, J. Wallenfeldt, A. Zeidan, and A. Zelazko, 2019, Encyclopedia Britannica, https://www.britannica.com/; accessed April 29, 2019.

Bagnold, R. A., 1941, The Physics of Blown Sand and Desert Dunes, London: Methuen.

Bevis, K. A., 2013, In the Playground of Giants, http://intheplaygroundofgiants.com/geology-basics-2/an-introduction-to-physical-geology/figure-29-migration-of-dunes-and-ripples/; accessed April 2019.

Blinn, J. F., August 1978, "Simulation of Wrinkled Surfaces", Computer Graphics, Vol. 12 (3), pp. 286-292 SIGGRAPH-ACM.

Breed, W. J., A. Warren, C. S. Breed, 2019, Sand dune, https://www.britannica.com/science/sand-dune, accessed Apr 3, 2019.

Campbell-Stone, E., R. Lynds, C. Frost, T. P. Becker, B. Diem, 2011, The Wyoming carbon underground storage project: Geologic characterization of the Moxa Arch and Rock Springs Uplift, Energy Procedia, **4**, 4656-4663.

Chan, M. A., and A. W. Archer, 2000, Cyclic eolian stratification on the Jurassic Navajo Sandstone, Zion National Park: Periodicities and implications for paleoclimate, in Sprinkel, D. A., Chidsey, T. C., Jr., and Anderson, P. B., eds., Geology of Utah's Parks and Monuments, **28**: Utah Geological Association Publication, 607–617.

Chopra, S., and K. J. Marfurt, 2010, Integration of coherence and volumetric curvatures images: The Leading Edge, **29,** 1092–1107.

Chopra, S., K. J. Marfurt, 2007, Seismic attributes for prospect identification and reservoir characterization: SEG Geophysical Developments No. 11. doi.org/10.1190/1.9781560801900

Cook, D., P. Constance, S. Singleton, P. Harris, 2019, Introduction to special section: Seismic data conditioning, Society of Exploration Geophsysicists, **4**, Issue 2, https://doi.org/10.1190/INT-2016-0314-SPSEINTRO.1

Cao, Z., J. C. Bancroft, 2004, Multiple attenuation by semblance weighted Radon transform, **16**, CREWES Research Report.

Faller, J. E., A. H. Cook, K. L. Nordtvedt, 2019, Gravity, https://www.britannica.com/science/gravity-physics; accessed April 29, 2019.

Fehmers, G., F. W. Höecker, 2003, Fast structural interpretation with structure-oriented filtering: Geophysics, **68**, 1286-1293.

GDallimore, 2010, https://en.wikipedia.org/wiki/Bump_mapping#/media/File:Bump-map-demo-full.png; accessed April 30, 2019.

Google Maps, 2019, https://www.google.com/maps; accessed March 15, 2019.

Grana, D., S. Verma, J. Pafeng, X. Lang, H. Sharma, W. Wu, E. Campbell-Stone, K. Ng, V. Alvarado, S. Mallick, and J. Kaszuba, 2017, A rock physics and seismic reservoir characterization study of the Rock Springs Uplift, a carbon dioxide sequestration site in Southwestern Wyoming: International Journal of Greenhouse Gas Control, **63**, 296-309. https://doi.org/10.1016/j.ijggc.2017.06.004

Kulyapin, P., and T. F. Sokolova, 2014, A Case Study about Integrated Petrofacies Characterization and Interpretation of Depositional Environment of the Bakken Shale in

the Williston Basin, North America Formation Evaluation and Rock Physics Modeling of the Bazhenov Shale: Petrophysics, **55**, no. 3, 211–218.

Kuwahara, M., K. Hachimura, S. Eiho, and M. Kinoshita, 1976, Digital processing of biomedical images: Plenum Press, 187–203.

Lindquist, S. J., 1983, Nugget Sandstone formation reservoir characteristics affecting production in the overthrust belt of Southwestern Wyoming: Society of Petroleum Engineers, SPE-10993-PA, **35**, 1355-1365. doi:10.2118/10993-PA

Loope, D. B. and C. M. Rowe, 2003, Long-lived pluvial episodes during deposition of the Navajo Sandstone: The Journal of Geology, **111**, 223–232.

Luo, Y., S. al-Dossary, and M. Marhoon, 2002, Edge-preserving smoothing and applications: The Leading Edge, **21**, 136–158.

Malin, M. C., M. J. S. Belton, M. H. Carr, 2019, Mars, https://www.britannica.com/place/Mars-planet; accessed April 29, 2019.

Mallick, S., and S. Adhikari, 2015, Amplitude-variation-with-offset and prestack-waveform inversion: A direct comparison using a real data example from the Rock Springs Uplift, Wyoming, USA: Geophysics, **80,** no. 2, B45-B59.

Matos, M. C., P. Léo Osorio, and P. R. Johann, 2007, Unsupervised seismic facies analysis using wavelet transform and self-organizing maps: Geophysics, **72**, no. 1, P9-P21. https://doi.org/10.1190/1.2392789

Mikkelsen, M., 2008, Simulation of Wrinkled Surfaces Revisited, image.diku.dk/projects/media/morten.mikkelsen.08.pdf; accessed April 29, 2019.

Mitchell, W. K., and R. J. Nelson, 1988, A Practical Approach to Statistical Log Analysis, Paper S, Transactions: SPWLA 29th Annual Logging Symposium, SPWLA-1988-S.

Moss, B., and R. Harrison, 1985, Statistically Valid Log Analysis Method Improves Reservoir Description: SPE Offshore Europe annual meeting, SPE-13981. DOI: http://dx.doi.org/10.2118/13981-MS.

National Park Services, 2018, Appalachian Paleogeography, https://www.nature.nps.gov/geology/education/education_graphics.cfm; accessed April 29, 2019.

Olsen, P., Sand Dunes of the Southwest, http://sand.xboltz.net/types.html; accessed Apr 12, 2019.

Parrish, J. T., and F. Peterson, 1988, Wind directions predicted from global circulation models and wind directions determined from eolian sandstones of the western United States - a comparison: Sedimentary Geology, **56**, 261-282.

Picard, M. D., 1977, Petrology of the Jurassic Nugget Sandstone, Northeast Utah and Southwest Wyoming: 29th Annual Field Conference, Wyoming Geological Association, 239-258.

Qi, J., F. Li, and K. J. Marfurt, 2017, Multiazimuth coherence: Geophysics, **82**, no. 6, O83-O89. https://doi.org/10.1190/geo2017-0196.1

Rider, M. H., M. Kennedy, 2011, The Geological Interpretation of Well Logs, ISBN 10: 0954190688 ISBN 13: 9780954190682.

Roy, A., B. L. Dowdell, and K. J. Marfurt, 2013, Characterizing a Mississippian tripolitic chert reservoir using 3D unsupervised and supervised multiattribute seismic facies analysis: An example from Osage County, Oklahoma: Interpretation, **1**, no. 2, SB109-SB124. https://doi.org/10.1190/INT-2013-0023.1

Saraswat, P., and M. K. Sen, 2012, Artificial immune-based self-organizing maps for seismic-facies analysis: Geophysics, **77**, no. 4, O45-O53.

Savre, W. C., 1963, Determination of a More Accurate Porosity andMineral Composition in Complex Lithologies with the use of the Sonic, Neutron, and Density Surveys: Journal of Petroleum Technology, Paper SPE-617, **15**, no. 6, 945–959.

Schlumberger Seismic Attribute Analysis, https://www.software.slb.com/products/petrel/petrel-geophysics/multitrace-attribute; accessed March 15 2019.

SEG, 2019, https://wiki.seg.org/wiki/Pickett_plot; accessed April 30, 2019.

Sheriff, R. E., 2002, Encyclopedic Dictionary of Applied Geophysics (4 ed.): Society of Exploration Geophysicists, ISBN 1-56080-118-2.

Silva, Celina C., C. S. Marcolino, and F. D. Lima, 2005, Automatic fault extraction using ant tracking algorithm in the Marlim South Field, Campos Basin: 75th Annual International Meeting, SEG, Expanded Abstracts, 857-860.

Surdam, R. C., 2013, Geological CO_2 storage characterization: The key to deploying clean fossil energy technology: Springer.

Verma, S., E. Campbell-Stone, H. Sharma, S. Mallick, D. Grana, 2016, Seismic attribute illumination of the Moxa Arch: A probable site for carbon sequestration: 86th Annual International Meeting, SEG, Expanded Abstracts, 1874-1878.

Verma, S., S. Bhattacharya, B. Lujan, D. Agrawal, S. Mallick, 2018, Delineation of Early Jurassic aged sand dunes and paleo-wind direction in southwestern Wyoming using seismic attributes, inversion, and petrophysical modeling: Journal of Natural Gas Science and Engineering, **60**, P1-10.

Xingxing, Z., L. Tingting, S. Yue, and Z. Yanqi, 2015, The Application of Fracture Interpretation Technology Based on Ant Tracking in Sudeerte Oilfield, Acta Geologica Sinica (English Edition), 89 (supp.): 437-438.

Zhao, T., J. Zhang, F. Li, and K. J. Marfurt, 2016, Characterizing a turbidite system in Canterbury Basin, New Zealand, using seismic attributes and distance-preserving self-organizing maps : Interpretation, **4,** no. 1, SB79-SB89. https://doi.org/10.1190/INT-2015-0094.1